CrossMark

J. Fluid Mech. (2021), *vol*. 907, A35. © The Author(s), 2020.
Published by Cambridge University Press
doi:10.1017/jfm.2020.775

Evolution of a shock generated by an impulsively accelerated, sinusoidal piston

N. Shen[1],†, **D. I. Pullin**[1], **R. Samtaney**[2] **and V. Wheatley**[3]

[1]Graduate Aerospace Laboratories, California Institute of Technology, Pasadena, CA 91125, USA

[2]Mechanical Engineering, Physical Science and Engineering Division, King Abdullah University of Science and Technology, Thuwal 23955-6900, Saudi Arabia

[3]School of Mechanical and Mining Engineering, The University of Queensland, St Lucia, QLD 4072, Australia

(Received 30 April 2020; revised 1 August 2020; accepted 9 September 2020)

We consider the evolution of a shock wave generated by an impulsively accelerated, two-dimensional, almost planar piston with a sinusoidally corrugated surface of amplitude ϵ. We develop a complex-variable formulation for a nonlinear theory of generalized geometrical shock dynamics (GGSD) (Best, *Shock Waves*, vol. 1, issue 4, 1991, pp. 251–273; Best, *Proc. R. Soc. Lond.* A, vol. 442, 1993, pp. 585–598) as a hierarchical expansion of the Euler equations that can be closed at any order. The zeroth-order truncation of GGSD is related to the equations of Whitham's geometrical shock dynamics (GSD), while higher-order corrections incorporate non-uniformity of the flow immediately behind the piston-driven shock. Numerical solutions to GGSD systems up to second order are coupled to an edge-detection algorithm in order to investigate the hypothesized development of a shock-shape curvature singularity as the rippled shock evolves. This singular behaviour, together with the simultaneous development of a Mach-number discontinuity, is found at all orders of the GGSD hierarchy for both weak and strong shocks. The critical time at which a curvature singularity occurs converges as the order of the GGSD system increases at fixed ϵ, and follows a scaling inversely proportional to ϵ at sufficiently small values. This result agrees with the weakly nonlinear GSD analysis of Mostert *et al.* (*J. Fluid Mech.*, vol. 846, 2018, pp. 536–562) for a general Mach-number perturbation on a planar shock, and suggests that this represents the universal behaviour of a slightly perturbed, planar shock.

Key words: gas dynamics, shock waves, nonlinear instability

1. Introduction

The dynamics of shock waves generated by the steady motion of a two-dimensional planar piston with a corrugated surface has been a classical hydrodynamic problem spanning over 60 years from the original work of Freeman (1955) to the more recent analysis of Bates (2015). The focus here concerns the stability of a rippled shock, which can be dynamically relevant to astrophysical phenomena (Maxwell, Dryer &

† Email address for correspondence: nshen@caltech.edu

https://doi.org/10.1017/jfm.2020.775 Published online by Cambridge University Press

McIntosh 1985; Drake *et al.* 1998), inertial confinement fusion applications (Matsui *et al.* 1999; Lindl *et al.* 2014), Bose–Einstein condensates and nonlinear optics (Hoefer, Ablowitz & Engels 2008). It has long been known that planar gaseous shock waves are linearly stable, that is, small perturbations along the shock surface decay over time following a power law (Lighthill 1949, 1950; Freeman 1955, 1957; Zaidel 1967; Van Moorhem & George 1975). The predictions of linear analysis are supported by the pioneering experiments of Lapworth (1959) and Briscoe & Kovitz (1968). But the experiments do display noticeable singular flow behaviour associated with the formation of a triple point, or Mach stem, on the shock front that cannot be explained by linear theory.

The dynamics of a triple point on a strongly perturbed shock was modelled by Whitham (1957), using his nonlinear theory of geometrical shock dynamics (GSD), as a shock on a shock or a 'shock–shock' that propagates transversely along the shock profile. The cellular structure of Mach stems ubiquitously observed in detonation waves (Strehlow & Fernandes 1965; Courant & Friedrichs 1999) has motivated a number of theoretical investigations of the spontaneous formation of triple points (Majda & Rosales 1983; Clavin & Denet 2002; Faria, Kasimov & Rosales 2015). Shock instabilities are also reported in non-reacting flows associated with perturbations of various origin. The nonlinear analysis of Clavin (2013) shows the formation of a singularity in the slope of a wrinkled shock produced by a shock–vortex interaction, under the distinguished limit where the shock Mach number becomes infinite while the specific heat ratio of the gas approaches unity. A two-stage description of the shock evolution and an order-of-magnitude estimate for the Mach-stem formation time was provided. Later, the shock-tube experiment of Denet *et al.* (2015) and the direct numerical simulations of Lodato, Vervisch & Clavin (2016, 2017) confirmed the triple-point formation of a shock reflected off a wavy wall, but did not relate the formation time to the initial perturbation size of the wall. Wan *et al.* (2017) investigated numerically and experimentally the triple-point trajectory due to shock interaction with a water wedge. Mostert *et al.* (2018*a*,*b*) hypothesized a sinusoidal perturbation in the Mach-number distribution for both initially flat and cylindrical shock geometry, finding that a shock curvature singularity, as a prelude to the formation of a triple point, occurs at a critical time τ_c that is inversely proportional to the initial perturbation amplitude, ϵ. This result is obtained analytically via weakly nonlinear Fourier analysis using Whitham's GSD approximation.

The strict GSD framework of Mostert *et al.* (2018*a*) first neglects the non-uniform effects of flow behind the shock carried by the C^+ characteristics. Second, the physical origin of the shock perturbation is not well defined owing to the restriction posed by the A–M relation (see our (2.9)) on the initial conditions of the shock-shape and Mach-number profiles. In the present study, we address these issues by applying the generalized geometrical shock dynamics (GGSD) formulation, developed by Best (1991, 1993) as a hierarchical expansion of the Euler equations that can be closed at any order. The GGSD systems relaxes the A–M relation while specifically incorporating the non-uniformity of the flow immediately behind the shock into its dynamical description in terms of evolution equations for higher-order derivatives of the primitive flow variables. Katko *et al.* (2020) showed that, owing to the inclusion of flow non-uniformity, the GGSD model successfully captures the analytical solution for the expansion of a blast wave in comparison with the GSD result.

Adopting the GGSD theory, we analyse the specific problem of a shock generated by a two-dimensional impulsive piston with a sinusoidally corrugated surface, in complex coordinates. The linear stability of a piston-driven shock was also investigated by Bates

https://doi.org/10.1017/jfm.2020.775 Published online by Cambridge University Press

(2012, 2015), who found an unstable region of the D'yakov parameter (D'yakov 1954) for gases of arbitrary equation of state, where a small perturbation on the shock front grows in time. Presently, we focus on an ideal-gas equation of state and propose a perturbation ansatz of a different nature where unstable modes are controlled by the intrinsic shock nonlinearity that ultimately leads to the spontaneous formation of a curvature singularity, detected numerically as a discontinuity of the Mach-number distribution along the shock. The critical time at which a singularity occurs converges as the order of the GGSD system increases from zero to two, and the inverse power law, $\tau_c \propto 1/\epsilon$, established by Mostert *et al.* (2018*a*), holds universally true with the present inclusion of the non-uniform effects of the shocked flow.

The remainder of this paper is organized as follows. We first discuss in § 2 the approximation error of GSD compared to the two-dimensional Euler equations, and introduce the GGSD expansion that improves the GSD theory. The analysis parallels Best (1993) but utilizes a different definition of the shock velocity. Evolution of a periodically perturbed planar shock is formulated in § 3 using complex variables. The zeroth-, first- and second-order truncated GGSD models are derived explicitly in the strong- and weak-shock limits as closed systems of partial differential equations that can be solved numerically using simple technique such as the method of lines. A linear stability analysis is also given in § 3. We then specialize in § 4 to the motion of a shock generated by a corrugated piston of sinusoidal surface being impulsively accelerated to a steady velocity. The necessary initial conditions required to integrate the GGSD systems for this shock are derived. These require shock-jump conditions for gradients of physical quantities. Then § 5 presents numerical results that characterize the shock-shape curvature singularity formation, and demonstrate the inverse power law that predicts the onset of triple points. Finally, conclusions are drawn in § 6.

2. Generalized geometrical shock dynamics

We begin by reviewing the GSD framework (Whitham 1957). Its limitations are identified in a direct comparison against the two-dimensional Euler equations. We then introduce GGSD developed by Best (1991), in order to improve the approximation error.

2.1. *Quasi-one-dimensional Euler equations*

The foundation for constructing the evolution equations for shocks in two-dimensional unsteady flow is the quasi-one-dimensional (1-D) Euler equations that describe flow of a polytropic gas down a tube of slowly varying cross-sectional area $A = A(x)$, along the propagation direction denoted by the spatial variable x. By averaging the inviscid compressible flow equations across the tube, one obtains the following approximation (Whitham 1957):

$$\left.\begin{aligned} \rho_t + u\rho_x + \rho u_x + \rho u\frac{A'(x)}{A(x)} &= 0,\\ \rho(u_t + uu_x) + p_x &= 0,\\ p_t + up_x - a^2(\rho_t + u\rho_x) &= 0. \end{aligned}\right\} \tag{2.1}$$

Here ρ, u and p are fluid density, velocity and pressure, respectively; $a = \sqrt{\gamma p/\rho}$ is the local sound speed for a perfect-gas equation of state, with γ the constant specific heat ratio; x and t are distance and time; the prime symbol denotes the derivative with respect to x;

https://doi.org/10.1017/jfm.2020.775 Published online by Cambridge University Press

and the subscripts t and x are used to signal their respective partial derivatives. Equations (2.1) can be written in characteristic form as

$$p_t + (u+a)p_x + \rho a(u_t + (u+a)u_x) + \rho a^2 u A'/A = 0, \quad \text{on } C^+ : \frac{\mathrm{d}x}{\mathrm{d}t} = u + a, \tag{2.2a}$$

$$p_t + (u-a)p_x - \rho a(u_t + (u-a)u_x) + \rho a^2 u A'/A = 0, \quad \text{on } C^- : \frac{\mathrm{d}x}{\mathrm{d}t} = u - a, \tag{2.2b}$$

$$p_t + up_x - a^2(\rho_t + u\rho_x) = 0, \quad \text{on } S : \frac{\mathrm{d}x}{\mathrm{d}t} = u. \tag{2.2c}$$

Denoting the trajectory of a shock propagating down the tube of uniform medium at rest by $x_s = x_s(t)$, its velocity is given by

$$\frac{\mathrm{d}x_s}{\mathrm{d}t} = a_0 M(t), \tag{2.3}$$

where a_0 is the upstream speed of sound and M is the shock Mach number. We define total time derivatives of ρ, u and p immediately behind the shock as their rates of change observed by a marker travelling with the shock, given by

$$\frac{\mathrm{D}\rho}{\mathrm{D}t} = \rho_t + a_0 M\rho_x, \quad \frac{\mathrm{D}u}{\mathrm{D}t} = u_t + a_0 M u_x, \quad \frac{\mathrm{D}p}{\mathrm{D}t} = p_t + a_0 M p_x. \tag{2.4a–c}$$

The following Rankine–Hugoniot (RH) conditions connect flow variables behind the shock to their upstream values via Mach number:

$$\left.\begin{aligned} u = F^u(M) &\equiv \frac{2a_0}{\gamma+1}\left(M - \frac{1}{M}\right), \\ \rho = F^\rho(M) &\equiv \frac{\rho_0(\gamma+1)M^2}{(\gamma-1)M^2+2}, \\ p = F^p(M) &\equiv \frac{\rho_0 a_0^2}{\gamma(\gamma+1)}(2\gamma M^2 - \gamma + 1), \\ a = F^a(M) &\equiv \frac{a_0\mu(2\gamma M^2 - \gamma + 1)}{(\gamma+1)M}, \end{aligned}\right\} \tag{2.5}$$

where ρ_0 is the upstream fluid density, and

$$\mu = \sqrt{\frac{(\gamma-1)M^2+2}{2\gamma M^2 - \gamma + 1}} \tag{2.6}$$

is the post-shock Mach number.

2.1.1. *The A–M relation*

By applying the RH conditions along the C^+ characteristics instead of the shock, namely, substituting (2.5) into (2.2*a*), Whitham (1957, 2011) obtained an expression for $M(A)$ that relates the shock Mach number, M, to the tube's local cross-sectional area, A. This so-called A–M relation gives the basis of the GSD theory. Here we attempt to

https://doi.org/10.1017/jfm.2020.775 Published online by Cambridge University Press

recover the A–M relation using a different method. With (2.1) and (2.4*a–c*) combined, all six partial derivatives, $p_t,\ p_x,\ u_t,\ u_x,\ \rho_t$ and ρ_x, can be solved from the resulting six linear equations. In particular, we have

$$\left.\begin{aligned} p_t &= \frac{a_0 M\rho u a^2(a_0M-u)A' + A\left[a^2\left(a_0M\rho\dfrac{\mathrm{D}\rho}{\mathrm{D}t}+\dfrac{\mathrm{D}p}{\mathrm{D}t}\right)+u\dfrac{\mathrm{D}p}{\mathrm{D}t}(a_0M-u)\right]}{A[a^2-(u-a_0M)^2]},\\ u_t &= \frac{a_0 M\rho u a^2A' + A\left[\rho\dfrac{\mathrm{D}u}{\mathrm{D}t}(a^2+u(a_0M-u))+a_0M\dfrac{\mathrm{D}p}{\mathrm{D}t}\right]}{A\rho[a^2-(u-a_0M)^2]}. \end{aligned}\right\} \tag{2.7}$$

Substituting (2.7) into the expression $(p_t+\rho a u_t)$ and using the identity $\mathrm{D}/\mathrm{D}t = (\mathrm{d}M/\mathrm{d}t)(\mathrm{d}/\mathrm{d}M)$ then gives an equation from which $\mathrm{d}M/\mathrm{d}t$ can be solved, producing

$$\left(\frac{\mathrm{d}p}{\mathrm{d}M}+\rho a\frac{\mathrm{d}u}{\mathrm{d}M}\right)\frac{\mathrm{d}M}{\mathrm{d}t} = -\left[\frac{a_0M\rho a^2uA'}{(a+u)A}+\left(\frac{a_0M}{a+u}-1\right)(p_t+\rho a u_t)\right], \tag{2.8}$$

where $\mathrm{d}p/\mathrm{d}M$, $\mathrm{d}u/\mathrm{d}M$, ρ, a and u are known as functions of M, from (2.5).

In Whitham's (1957) development of the A–M relation, it is argued that $|p_t+\rho a u_t|$ must be small to justify the use of the 'characteristic rule'. In the current formulation, this is equivalent to neglecting the last term in (2.8), noting that the component $|a_0M/(a+u)-1|$ is uniformly bounded for all $M\in(1,\infty)$. As a result, using $\mathrm{d}A/\mathrm{d}x = (\mathrm{d}A/\mathrm{d}t)/(a_0M)$, the A–M relation follows:

$$\frac{1}{A}\frac{\mathrm{d}A}{\mathrm{d}M} = \frac{-M}{M^2-1}\left(1+\frac{2(1-\mu^2)}{(\gamma+1)\mu}\right)\left(1+2\mu+\frac{1}{M^2}\right), \tag{2.9}$$

which can then be integrated to give $M=M(A)$, up to a multiplying constant.

One useful feature of the present derivation of (2.9) is that, compared to Whitham's (1957, 2011) original 'characteristic rule', which essentially assumes that the non-uniform flow effect behind the shock carried by the C^+ characteristics does not modify the shock motion, the error associated with this assumption can be exactly quantified. Here, the neglected term is the product of two terms, where $|a_0M/(a+u)-1|$, as a function of M only, measures the geometrical closeness between the C^+ characteristics and the shock, while $|p_t+\rho a u_t|$ captures the non-uniformity of the flow immediately behind the shock.

2.2. *Two-dimensional Euler equations*

We can extend the quasi-1-D theory to two-dimensional (2-D) flows. A 2-D shock-shape profile must be specified in terms of an intrinsic coordinate that labels points along the shock. Following Whitham's (1957, 2011) GSD theory, we spatially parametrize points on the shock with the parameter β. This is defined as a continuous, monotonically increasing variable along the shock such that a point with fixed β is instantaneously moving with velocity (in the laboratory frame) that is normal to the shock. This can be taken as the present definition of the 'shock velocity'. Conceptually, it is related to the quasi-1-D concept that the shock moves along 'ray tubes' that are locally normal to the shock front.

For a given β at time t, we set up a laboratory-fixed local Cartesian coordinate system shown in figure 1, whose origin sits on the shock point defined by β. The positive x-direction aligns with the instantaneous shock velocity at the origin and the positive

https://doi.org/10.1017/jfm.2020.775 Published online by Cambridge University Press

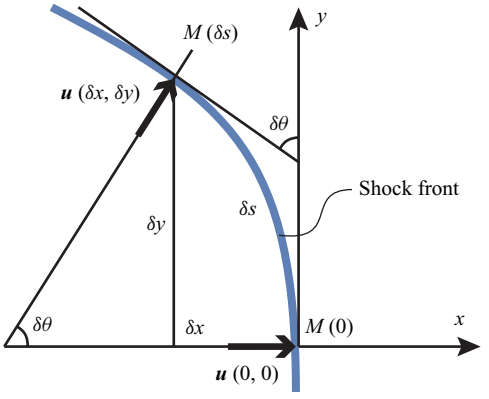


FIGURE 1. Local Cartesian coordinates fixed at a point on the shock normal (x-direction) and tangential (y-direction) to the curve. Downstream velocity vectors and Mach numbers are shown at the origin and a differential nearby point at $(\delta x, \delta y)$, whose arclength is δs.

y-direction corresponds to an increase of β along the shock. The Mach-number profile along the shock may be parametrized as a function of arclength, s, measured from the origin in the positive y-direction. In GSD, s and β are related by defining the normalized ray-tube area A as

$$A = \frac{\mathrm{d}s}{\mathrm{d}\beta}. \tag{2.10}$$

The flow that defines the shock is governed by the 2-D Euler equations:

$$\rho_t + u\rho_x + v\rho_y + \rho(u_x + v_y) = 0, \tag{2.11a}$$

$$\rho(u_t + uu_x + vu_y) + p_x = 0, \tag{2.11b}$$

$$\rho(v_t + uv_x + vv_y) + p_y = 0, \tag{2.11c}$$

$$p_t + up_x + vp_y + \gamma p(u_x + v_y) = 0. \tag{2.11d}$$

2.2.1. *Tangential derivatives*

In order to obtain an evolution equation analogous to (2.8) that governs the shock motion in two dimensions, all partial derivatives of the flow variables present in (2.11) must be evaluated immediately behind the shock. In particular, this can be done explicitly for the tangential derivatives, i.e. those with respect to y. At the origin, we have, just downstream of the shock, x and y components of flow velocity (in the laboratory frame), density and pressure given by

$$\left.\begin{aligned} u(0,0) = F^u(M(0)), \quad v(0,0) = 0, \\ \rho(0,0) = F^\rho(M(0)), \quad p(0,0) = F^p(M(0)). \end{aligned}\right\} \tag{2.12}$$

At a nearby point on the shock $(\delta x, \delta y)$ with arclength $\delta s = \sqrt{\delta x^2 + \delta y^2}$, making a tangent angle of $\delta\theta$ with the y-axis (figure 1), these flow quantities become

$$\left.\begin{aligned} u(\delta x, \delta y) = F^u(M(\delta s))\cos(\delta\theta), \quad v(\delta x, \delta y) = F^u(M(\delta s))\sin(\delta\theta), \\ \rho(\delta x, \delta y) = F^\rho(M(\delta s)), \quad p(\delta x, \delta y) = F^p(M(\delta s)), \end{aligned}\right\} \tag{2.13}$$

https://doi.org/10.1017/jfm.2020.775 Published online by Cambridge University Press

where the Mach number has the Taylor expansion

$$M(\delta s) = M(0) + \left.\frac{\mathrm{d}M}{\mathrm{d}s}\right|_{(0,0)} \delta s + o(\delta s). \tag{2.14}$$

To proceed we make use of the following three limits:

$$\lim_{\delta y\to 0} \delta x/\delta y = 0, \quad \lim_{\delta y\to 0} \delta s/\delta y = 1, \quad \lim_{\delta y\to 0} \delta\theta/\delta y = \kappa, \tag{2.15a–c}$$

where κ is the signed curvature of the shock at the origin. As a result, (2.13) are further Taylor expanded as:

$$\left.\begin{aligned} u(0,0) + \left.\frac{\partial u}{\partial y}\right|_{(0,0)} \delta y &= F^u(M(0)) + \left[\frac{\mathrm{d}F^u}{\mathrm{d}M}\frac{\mathrm{d}M}{\mathrm{d}s}\right]_{(0,0)} \delta y + o(\delta y), \\ v(0,0) + \left.\frac{\partial v}{\partial y}\right|_{(0,0)} \delta y &= F^u(M(0))\delta\theta + o(\delta y), \\ \rho(0,0) + \left.\frac{\partial \rho}{\partial y}\right|_{(0,0)} \delta y &= F^\rho(M(0)) + \left[\frac{\mathrm{d}F^\rho}{\mathrm{d}M}\frac{\mathrm{d}M}{\mathrm{d}s}\right]_{(0,0)} \delta y + o(\delta y), \\ p(0,0) + \left.\frac{\partial p}{\partial y}\right|_{(0,0)} \delta y &= F^p(M(0)) + \left[\frac{\mathrm{d}F^p}{\mathrm{d}M}\frac{\mathrm{d}M}{\mathrm{d}s}\right]_{(0,0)} \delta y + o(\delta y). \end{aligned}\right\} \tag{2.16}$$

Substituting (2.12) into (2.16) and applying the $\delta y \to 0$ limit then gives the desired tangential derivatives at the origin,

$$\left.\begin{aligned} \frac{\partial u}{\partial y} &= \frac{\mathrm{d}F^u}{\mathrm{d}M}\frac{\mathrm{d}M}{\mathrm{d}s}, \quad \frac{\partial v}{\partial y} = F^u(M)\kappa, \\ \frac{\partial \rho}{\partial y} &= \frac{\mathrm{d}F^\rho}{\mathrm{d}M}\frac{\mathrm{d}M}{\mathrm{d}s}, \quad \frac{\partial p}{\partial y} = \frac{\mathrm{d}F^p}{\mathrm{d}M}\frac{\mathrm{d}M}{\mathrm{d}s}, \end{aligned}\right\} \tag{2.17}$$

where we may write

$$\frac{\mathrm{d}M}{\mathrm{d}s} = \frac{\mathrm{d}M}{\mathrm{d}\beta}\frac{\mathrm{d}\beta}{\mathrm{d}s} = \frac{1}{A}\frac{\mathrm{d}M}{\mathrm{d}\beta}. \tag{2.18}$$

Using (2.10) and (2.18), the derivatives in (2.17) can be calculated at time t provided both the shock-shape and Mach-number profiles are known functions of β.

2.2.2. *Time and normal derivatives*

Since the shock marker located at the origin at time t has velocity normal to itself, the time and normal derivatives of flow variables immediately behind the shock are related

https://doi.org/10.1017/jfm.2020.775 Published online by Cambridge University Press

through the total derivatives:

$$\frac{\mathrm{D}u}{\mathrm{D}t} = \frac{\mathrm{d}F^u}{\mathrm{d}M}\left(\frac{\partial M}{\partial t}\right)_\beta = \frac{\partial u}{\partial t} + a_0 M\frac{\partial u}{\partial x}, \tag{2.19a}$$

$$\frac{\mathrm{D}v}{\mathrm{D}t} = 0 = \frac{\partial v}{\partial t} + a_0 M\frac{\partial v}{\partial x}, \tag{2.19b}$$

$$\frac{\mathrm{D}\rho}{\mathrm{D}t} = \frac{\mathrm{d}F^\rho}{\mathrm{d}M}\left(\frac{\partial M}{\partial t}\right)_\beta = \frac{\partial \rho}{\partial t} + a_0 M\frac{\partial \rho}{\partial x}, \tag{2.19c}$$

$$\frac{\mathrm{D}p}{\mathrm{D}t} = \frac{\mathrm{d}F^p}{\mathrm{d}M}\left(\frac{\partial M}{\partial t}\right)_\beta = \frac{\partial p}{\partial t} + a_0 M\frac{\partial p}{\partial x}. \tag{2.19d}$$

In addition, all the partial derivatives discussed so far satisfy the 2-D Euler equations (2.11). Therefore, substituting (2.12) and (2.17) into (2.11), together with (2.19) gives eight linear equations for eight unknowns, i.e. the x and t partial derivatives of u, v, ρ and p. This process is analogous to the derivation of (2.7) for the quasi-1-D problem. In particular, the solution yields

$$\left.\begin{aligned}
\frac{\partial u}{\partial t} &= \frac{\rho(a^2-u^2)\left(\dfrac{\partial M}{\partial t}\right)_\beta \dfrac{\mathrm{d}u}{\mathrm{d}M} + a_0 M\left[\left(\dfrac{\partial M}{\partial t}\right)_\beta\left(\rho u\dfrac{\mathrm{d}u}{\mathrm{d}M} + \dfrac{\mathrm{d}p}{\mathrm{d}M}\right) + \kappa\rho a^2 u\right]}{\rho[a^2-(u-a_0M)^2]},\\
\frac{\partial p}{\partial t} &= \frac{u(a_0M-u)\left(\dfrac{\partial M}{\partial t}\right)_\beta \dfrac{\mathrm{d}p}{\mathrm{d}M} + a^2\left[\left(\dfrac{\partial M}{\partial t}\right)_\beta\left(\dfrac{\mathrm{d}p}{\mathrm{d}M} + a_0\rho M\dfrac{\mathrm{d}u}{\mathrm{d}M}\right) + a_0\kappa\rho u M(a_0M-u)\right]}{a^2-(u-a_0M)^2}.
\end{aligned}\right\} \tag{2.20}$$

2.3. *Geometrical equivalence*

Using (2.20) to expand the expression $(p_t + \rho a u_t)$ then gives, at any β and t,

$$\left(\frac{\partial M}{\partial t}\right)_\beta = -\frac{\dfrac{\kappa a_0 M\rho a^2 u}{(a+u)} + \left(\dfrac{a_0 M}{a+u} - 1\right)\left(\dfrac{\partial p}{\partial t} + \rho a\dfrac{\partial u}{\partial t}\right)}{\dfrac{\mathrm{d}p}{\mathrm{d}M} + \rho a\dfrac{\mathrm{d}u}{\mathrm{d}M}}. \tag{2.21}$$

An expedited route to arrive at (2.21) is to observe that, because $v = 0$, the momentum equation (2.11*c*) for v decouples from the rest of equations (2.11). Also comparing (2.11) to (2.1), and (2.4*a–c*) to (2.19), the only difference is that A'/A in (2.1) is replaced by κ in (2.11). As a result, (2.21) is directly analogous to (2.8).

We can conclude that GSD in its complete form given by (2.8) with the $(p_t + \rho a u_t)$ term retained is equivalent to 2-D Euler if and only if

$$\kappa = \frac{A'}{A} = \frac{1}{a_0 M A}\left(\frac{\partial A}{\partial t}\right)_\beta. \tag{2.22}$$

https://doi.org/10.1017/jfm.2020.775 Published online by Cambridge University Press

By defining A in 2-D flow as the normalized ray-tube area given in (2.10), Whitham (2011, equation (8.59)) showed, using the standard α–β curvilinear coordinates in GSD, that

$$\frac{\partial \theta}{\partial \beta} = \frac{1}{M}\frac{\partial A}{\partial \alpha}, \tag{2.23}$$

where $\alpha \equiv a_0 t$ is defined as a time-like label for the position of a shock along a ray corresponding to constant β. Equation (2.23) can be shown to be equivalent to (2.22) by noting that $\mathrm{d}s = A\,\mathrm{d}\beta$. For example, the geometrical equivalence for a converging/diverging cylindrical shock of radius r is trivially verified by identifying $A = A(r) = 2\pi r$, and thus $A'/A = 1/r = \kappa$.

Notably, the geometrical equivalence between the evolution of shocks in quasi-1-D and genuine 2-D flows is invariant with respect to the Cartesian coordinates used in § 2.2. Best (1993) observed this equivalence and derived an alternative to the original GGSD theory (Best 1991) resulting from defining the shock velocity to include the local flow velocity component that is tangential to the shock at a time instant. In contrast, in § 2.2, we spatially parametrize the shock using β, which labels shock points that propagate locally normal to the shock front. This difference illustrates the somewhat arbitrary definition of the shock velocity. The formulations are physically equivalent. An immediate implication of the geometrical equivalence is that it suffices to consider the quasi-1-D formulation alone in order to construct the shock dynamics in two dimensions, by effectively stacking ray tubes of normalized area A. We can thus proceed in the following analysis without invoking the 2-D Euler equations.

2.4. *A hierarchical expansion of the Euler equations*

As shown in §§ 2.1.1 and 2.3, compared to the true Euler equations, the non-uniform details of the flow behind the shock that is missing in the GSD approximation is entirely encapsulated in the quantity $(p_t + \rho a u_t)$. Therefore a suitable evolutionary model for such a quantity is desired to provide corrections to the GSD description. In the present study, we adapt the GGSD model proposed by Best (1991), which expands the Euler equations as a hierarchical system that can be closed at any order. A summary of Best's formulation is outlined here.

The construction begins with assuming sufficient smoothness of quasi-1-D flow and defining

$$Q_n \equiv \frac{\partial^{n-1}}{\partial t^{n-1}}\left(\frac{\partial p}{\partial t} + \rho a \frac{\partial u}{\partial t}\right), \quad n = 1, 2, \ldots, \tag{2.24}$$

evaluated immediately downstream of the shock. It is noted that Q_1 gives the non-uniformity measure, the quantity of interest. Computing the expansion of Q_n involves the following convenient differential operator,

$$\mathcal{F}^{i,j} \equiv \frac{\partial^{i+j}}{\partial x^i \partial t^j}, \quad i, j \in \{0, 1, 2, \ldots\}, \tag{2.25}$$

acting on the flow variables p, u, ρ and a. Let $\xi \in \{p, u, \rho\}$; then along the trajectory of the shock, the total derivative of ξ is given by

$$\frac{\mathrm{D}}{\mathrm{D}t}(\mathcal{F}^{i,j}[\xi]) = \mathcal{F}^{i,j+1}[\xi] + a_0 M \mathcal{F}^{i+1,j}[\xi]. \tag{2.26}$$

https://doi.org/10.1017/jfm.2020.775 Published online by Cambridge University Press

Further, the following identity for continuously differentiable functions A and B,

$$\mathcal{F}^{i,j}[AB] = \sum_{n=0}^{i}\sum_{m=0}^{j}\binom{i}{n}\binom{j}{m}\mathcal{F}^{n,m}[A]\mathcal{F}^{i-n,j-m}[B], \tag{2.27}$$

where $\binom{i}{n}$ and $\binom{j}{m}$ are the binomial operators, allows the Euler equations (2.2) to be differentiated by the operator $\mathcal{F}^{i,j}$. This, together with (2.26), forms six linear equations for six unknowns:

$$(\mathcal{F}^{i+1,j}[p],\ \mathcal{F}^{i+1,j}[u],\ \mathcal{F}^{i+1,j}[\rho],\ \mathcal{F}^{i,j+1}[p],\ \mathcal{F}^{i,j+1}[u],\ \mathcal{F}^{i,j+1}[\rho])^{\mathrm{T}}, \tag{2.28}$$

which can be solved analogously to the derivation of (2.7). The explicit solutions are found in equations (61)–(66) of Best (1991). Best's result can be viewed as extensions of the RH condition to the jump in partial derivatives of flow variables across a curved shock, which is a topic that has also been studied by Thomas (1947), Kanwal (1957), Pant (1969), Hornung (2010), Mölder (2016) and Emanuel (2016, 2019).

With (2.28) determined, it is then possible to prove by induction the following dependence relation for the partial derivatives:

$$\mathcal{F}^{0,0}[\xi] = \xi(M), \tag{2.29a}$$

$$\mathcal{F}^{i,j}[\xi] = \mathcal{F}^{i,j}[\xi]\left(M, Q_1, \ldots, Q_k, A'/A, \ldots, \frac{\mathrm{d}^{k-1}(A'/A)}{\mathrm{d}x^{k-1}}\right), \tag{2.29b}$$

for $k = i + j$, and $i, j \in \{0, 1, \ldots\}$. With some manipulations, (2.29) leads to

$$\frac{\mathrm{D}M}{\mathrm{D}t} = \frac{\mathrm{D}M}{\mathrm{D}t}(M, Q_1, A'/A), \tag{2.30a}$$

$$\frac{\mathrm{D}Q_{k+1}}{\mathrm{D}t} = \frac{\mathrm{D}Q_{k+1}}{\mathrm{D}t}\left(M, Q_1, \ldots, Q_{k+2}, A'/A, \ldots, \frac{\mathrm{d}^{k}(A'/A)}{\mathrm{d}x^{k}}\right). \tag{2.30b}$$

The explicit expansion of (2.30*a*) was earlier derived in (2.8) where only first-order partial derivatives of the flow variables were used. In general, higher-order partial derivatives are required to expand (2.30*b*) and give

$$\begin{aligned}\frac{\mathrm{D}Q_{k+1}}{\mathrm{D}t} = -\Bigg[&a_0 M\frac{\partial^{k+1}}{\partial t^{k+1}}\left(\frac{\rho a^2 u}{a+u}\right)\frac{A'}{A} + a_0 M\sum_{i=1}^{k+1}\binom{k+1}{i}\frac{\partial^i}{\partial t^i}\left(\frac{1}{a+u}\right)Q_{k-i+2}\\ &+ a_0 M\frac{\partial^k}{\partial t^k}\left(\frac{\partial(\rho a)}{\partial t}\frac{\partial u}{\partial x} - \frac{\partial(\rho a)}{\partial x}\frac{\partial u}{\partial t}\right) + \left(\frac{a_0 M}{a+u} - 1\right)Q_{k+2}\Bigg].\end{aligned} \tag{2.31}$$

Importantly, (2.29*b*) and (2.30*b*) show that the dependence of $\mathrm{D}Q_{k+1}/\mathrm{D}t$ upon derivatives of ξ of order $\leq k+1$ is fully specified by knowing M and Q_i of order $i \leq k+1$. Therefore, for a sequence of coupled nonlinear evolution equations described by (2.30) for $k = 1, \ldots, N$, closure can be achieved by truncating the term $[a_0 M/(a+u) - 1]Q_{N+2}$ in (2.31). This results in a closed system of $N+2$ nonlinear differential equations for the variables $M, Q_1, \ldots, Q_{N+1}$, which can be integrated in time provided the initial conditions for $M, Q_1, \ldots, Q_{N+1}$ are known.

For instance, it has been shown in § 2.1.1 that truncation at Q_1 in (2.30*a*) leads to the A–M relation in GSD. And by sampling Q_1 and its higher derivatives $Q_{i\geq 1}$,

https://doi.org/10.1017/jfm.2020.775 Published online by Cambridge University Press

at time $t = 0$, the non-uniformity of the initial flow behind the shock is described, which then evolves in time according to the expansion of the Euler equations. Similar to applying the 'characteristic rule' in GSD, where the C^+ characteristic is applied at the shock, the truncation error associated with the present higher-order approach is due to forcing the $\mathrm{D}Q_N/\mathrm{D}t$ equation along the C^+ characteristic at the shock.

The conditions for convergence of the Mach number M to the solution obtained from the full 2-D Euler equations as a function of t, when the truncation number N increases, remains an open problem that is addressed incompletely in Best (1991, 1993). We hypothesize that conditions for convergence may be problem-dependent. It is noted that Best's formulation certainly breaks down when the smooth flow assumption is violated, especially if additional discontinuous disturbances that originated downstream and carried by the C^+ characteristics overtake the shock. Such flow conditions are excluded in the present study.

3. Evolution of a periodic, perturbed planar shock

3.1. *A complex-variable formulation*

With the truncated GGSD equations established in § 2.4, we can now describe the motion of a slightly perturbed planar shock, parametrized periodically using ray-tube marker $\beta \in [0, 2\pi)$ (see § 2.2), by correctly replacing $A(x)$ in the quasi-1-D case with the normalized ray-tube area given in (2.10) for a 2-D shock. The 2π-periodic formulation is convenient for our application to a shock generated by a periodically corrugated piston in § 4. Following Mostert *et al.* (2018*a*), we describe the shock shape in a complex $z = x + \mathrm{i}y$ plane by $z = Z(\beta, t) = X(\beta, t) + \mathrm{i}Y(\beta, t)$.

By defining ray-tube markers along the shock whose velocity is locally normal to the shock curve, the kinematic equation for the shock profile reads as

$$\left(\frac{\partial Z}{\partial t}\right)_\beta = a_0 M(\beta, t)\hat{n}(\beta, t), \tag{3.1}$$

where $Z \in \mathbb{C}$ is the complex variable that describes the shock curve, a_0 is the upstream constant sound speed, M is the local Mach number and $\hat{n} \in \mathbb{C}$ is the unit normal vector aligned with the local shock velocity.

The complex shock profile Z is now decomposed into a steady flat shock of constant Mach number M_0 moving in the positive imaginary direction, and its perturbation,

$$Z = Z_0 + z(\beta, t), \quad Z_0 = \beta + \mathrm{i}a_0 M_0 t. \tag{3.2a,b}$$

It is noted that the unperturbed shock at $t = 0$ here lies on the real axis in the complex plane, and moves in the positive y-direction. This notation conventionally differs from the discussion in § 2.2.

Further, the unit normal vector, $\hat{n} = \mathrm{i}\hat{s}$, is obtained through a rotation of the unit tangent $\hat{s}$, given by

$$\hat{s} = \frac{1}{A(\beta, t)}\frac{\partial Z}{\partial \beta}, \tag{3.3}$$

where

$$A(\beta, t) = \left|\frac{\partial Z}{\partial \beta}\right| = \sqrt{\frac{\partial Z}{\partial \beta}\frac{\partial Z^*}{\partial \beta}} \tag{3.4}$$

https://doi.org/10.1017/jfm.2020.775 Published online by Cambridge University Press

is the normalized ray-tube area in the complex-variable formulation, following (2.10), and * denotes complex conjugate. The kinematic equation for the shock-profile perturbation then becomes

$$\frac{\partial z}{\partial t} = \mathrm{i}a_0 M_0 \left[\frac{M}{M_0} \left(1 + \frac{\partial z}{\partial \beta} \right) \left| 1 + \frac{\partial z}{\partial \beta} \right|^{-1} - 1 \right]. \tag{3.5}$$

3.2. *Zeroth-order GGSD system: GGSD-0*

In order to determine the evolution of the shock shape z, it remains to specify the dynamics of the Mach-number profile M, which can also be written in the perturbation form

$$M = M_0 + m. \tag{3.6}$$

Conveniently, using (2.21) with the help of (2.22) and (2.24), we have shown that the Euler equations dictate

$$\frac{\partial m}{\partial t} = -\frac{\dfrac{\rho a^2 u \Phi a_0 M}{(a+u)} + \left(\dfrac{a_0 M}{a+u} - 1 \right) Q_1}{\mathrm{d}p/\mathrm{d}M + \rho a (\mathrm{d}u/\mathrm{d}M)}, \tag{3.7}$$

where $\Phi \equiv (\partial A/\partial t)/(a_0 M A)$ and can be obtained by differentiating (3.4) using (3.1) as

$$\Phi = \Phi(Z) = -\left| \frac{\partial Z}{\partial \beta} \right|^{-3} \mathrm{Im} \left(\frac{\partial^2 Z}{\partial \beta^2} \frac{\partial Z^*}{\partial \beta} \right). \tag{3.8}$$

Now, by setting $Q_1 = 0$, (3.5) and (3.7) form a set of coupled nonlinear differential equations that describes the shock motion. Such a system corresponds to the zeroth-order truncation of the hierarchical GGSD equations introduced in § 2.4, which gives rise to the A–M relation seen in the GSD model.

There is a subtle difference between GSD and the zeroth-order GGSD system, henceforth referred to as GGSD-0. In GSD, the A–M relation, once determined with a unique integration constant, serves as a global constraint over the entire shock profile. For example, Mostert *et al.* (2018*a*) derived an expression for the Mach-number profile M for a planar shock that is completely determined by the local shock shape Z, namely, $M = M(Z)$. Consequently, (3.5) and (3.7) reduce and combine into a single equation for Z that governs the shock shape (see Mostert *et al.* (2018*a*), equation (2.9)). In contrast, by separating (3.5) and (3.7) as two independent evolution equations in GGSD-0, the A–M relation applies locally at a given β, allowing the integration constant to differ along the shock. The obvious benefit of such separation is that GGSD-0 is able to handle more general initial value problems that are forbidden in GSD, where the initial shock-shape and Mach-number profiles do not satisfy a global A–M relation everywhere on the shock. Nevertheless if the initial conditions are compatible with a global A–M relation, then GGSD-0 is identical to GSD.

3.2.1. *Strong- and weak-shock limits*

Here, we simplify (3.7) in the strong- and weak-shock limits, as $M \to \infty$ and $M \to 1$, respectively. This is achieved by utilizing the limiting forms of the RH conditions (2.5)

https://doi.org/10.1017/jfm.2020.775 Published online by Cambridge University Press

given by

$$u \sim \alpha_1 a_0 M, \quad p \sim \alpha_1 \rho_0 a_0^2 M^2, \quad \rho \sim \alpha_2 \rho_0, \quad a \sim \alpha_3 a_0 M, \tag{3.9a–d}$$

as $M \to \infty$, where $\alpha_{1,2,3}$ are constant functions of γ, given in table 1 in appendix A; and similarly,

$$u \sim 2\alpha_1 a_0 \varepsilon_w, \quad p \sim \rho_0 a_0^2 \left(\frac{1}{\gamma} + 2\alpha_1 \varepsilon_w\right), \quad \rho \sim \rho_0 (1 + 2\alpha_1 \varepsilon_w), \quad a \sim a_0 \left(1 + \frac{2\varepsilon_w}{\alpha_2}\right), \tag{3.10a–d}$$

where $\varepsilon_w \equiv M - 1$ and $\varepsilon_w \to 0$ defines the weak-shock limit. We note that appendix A contains lists of parameters that we use throughout the present study.

Evaluating (3.7) using (3.9*a–d*) and (3.10*a–d*), respectively, then yields

$$\left(\frac{\partial M}{\partial t}\right)_\beta = \begin{cases} -\zeta_1 a_0 \Phi M^2 + \dfrac{\zeta_2 Q_1}{\rho_0 a_0^2 M} + O(1/M^2), & M \to \infty, \\ -\dfrac{a_0 \Phi \varepsilon_w}{2} + \dfrac{Q_1 \varepsilon_w}{4\alpha_1 \rho_0 a_0^2} + O(\varepsilon_w^2), & \varepsilon_w \to 0, \end{cases} \tag{3.11}$$

where $\zeta_{1,2}$ are again constants listed in table 1 in appendix A. In this asymptotic form, it is assumed that Q_1 is at least of order $O(M^3)$ in the strong-shock limit, and of order $O(\varepsilon_w^0)$ in the weak-shock limit, for the correction term to be comparable in the respective leading-order expression. Although not necessary for the zeroth-order GGSD model, where the correction is neglected by letting $Q_1 = 0$, such assumptions about the magnitude of Q_1 will be shown to be essential for deriving the limiting expressions for higher-order GGSD models in the following sections.

For completeness, the zeroth-order GGSD systems in the strong- and weak-shock limits are given by the following closed system:

$$\frac{\partial Z}{\partial t} = \mathrm{i} a_0 M \frac{\partial Z}{\partial \beta} \left|\frac{\partial Z}{\partial \beta}\right|^{-1}, \quad \left(\frac{\partial M}{\partial t}\right)_\beta = \begin{cases} -\zeta_1 a_0 \Phi M^2, & M \to \infty, \\ -\dfrac{a_0 \Phi}{2}(M - 1), & M \to 1. \end{cases} \tag{3.12a,b}$$

3.3. *First-order GGSD system: GGSD-1*

As discussed in § 2.4, corrections to GGSD-0 can be made by including higher-order equations that capture the evolution of Q_1. In this section, we obtain the GGSD-1 model explicitly in the weak- and strong-shock limits.

The evolution of Q_1 following the shock trajectory in the quasi-1-D flow is governed by (2.31) with $k = 0$. Using the present complex-variable formulation, the total time derivative, $\mathrm{D}Q_1/\mathrm{D}t$, described by (2.31) directly equates to the partial time derivative tracing a fixed ray-tube marker β, namely, $(\partial Q_1/\partial t)_\beta$. Similarly, the full differential $\mathrm{d}x$ that appears in A' is now understood as the differential distance travelled by the shock in

https://doi.org/10.1017/jfm.2020.775 Published online by Cambridge University Press

the ray-tube direction, i.e.

$$\mathrm{d}x = a_0 M(\beta, t)\,\mathrm{d}t, \quad \frac{A'}{A} = \frac{1}{a_0 M A}\left(\frac{\partial A}{\partial t}\right)_\beta = \Phi, \tag{3.13a,b}$$

where Φ is given in (3.8). Now substituting (3.13*a*,*b*) into (2.31) yields

$$\left(\frac{\partial Q_1}{\partial t}\right)_\beta = -a_0 M\left[\frac{\partial}{\partial t}\left(\frac{\rho a^2 u}{a+u}\right)\Phi + \frac{\partial(\rho a)}{\partial t}\frac{\partial u}{\partial x} - \frac{\partial(\rho a)}{\partial x}\frac{\partial u}{\partial t} + \frac{\partial}{\partial t}\left(\frac{1}{a+u}\right)Q_1 + \left(\frac{1}{a+u} - \frac{1}{a_0 M}\right)Q_2\right]. \tag{3.14}$$

Expanding (3.14) and noting that $a = \sqrt{\gamma p/\rho}$ produces first-order partial derivatives of ρ, u and p with respect to t and x, which are found as a subset of solution (2.28), where $i = j = 0$. Therefore, in view of (2.29*b*), (3.14) is fully specified knowing M, Q_1 and Φ, except for the last term that contains Q_2. Hence truncation at $Q_2 = 0$ provides closure. GGSD-1 then comprises (3.5), (3.7) and (3.14) with $Q_2 = 0$.

3.3.1. *The weak-shock limit*

The full expansion of $\mathcal{F}^{0,1}[\xi^*]$ and $\mathcal{F}^{1,0}[\xi^*]$, where $\xi^* \in \{\rho, u, p, a\}$, can be obtained as a subset from the solution process to the arrival of (2.28). Using the asymptotic forms (3.10*a*–*d*) and (3.11), these first-order partial derivatives, listed in (B 1)–(B 4) of appendix B, simplify in the weak-shock limit as $\varepsilon_w = M - 1 \to 0$. It is noted that the leading-order behaviour of all eight partial derivatives in this limit relies on the assumption that $Q_1 \sim O(\varepsilon_w^0) \sim O(1)$, which is consistent with the observation made with (3.11) when $Q_1 \neq 0$ is allowed.

Substituting (3.10*a*–*d*) and (B 1)–(B 4) into (3.14) then gives the leading-order evolution of Q_1 in the weak-shock limit,

$$\left(\frac{\partial Q_1}{\partial t}\right)_\beta = \frac{Q_1}{2}\left(\frac{Q_1}{\alpha_1 \rho_0 a_0^2} - a_0\Phi\right) + Q_2\varepsilon_w + O(\varepsilon_w), \tag{3.15}$$

where the correction term $Q_2\varepsilon_w$ enters only if $Q_2 \sim O(1/\varepsilon_w)$ at least. However, closure of the GGSD system at first order demands $Q_2 = 0$; and therefore combining (3.5), (3.11) and (3.15) completes the weak-shock limiting GGSD-1 equations as follows:

$$\left.\begin{aligned} \frac{\partial Z}{\partial t} &= \mathrm{i}a_0 M\frac{\partial Z}{\partial \beta}\left|\frac{\partial Z}{\partial \beta}\right|^{-1}, \\ \frac{\partial M}{\partial t} &= \left(-\frac{a_0\Phi}{2} + \frac{Q_1}{4\alpha_1\rho_0 a_0^2}\right)(M-1), \\ \frac{\partial Q_1}{\partial t} &= \frac{Q_1}{2}\left(\frac{Q_1}{\alpha_1\rho_0 a_0^2} - a_0\Phi\right). \end{aligned}\right\} \tag{3.16}$$

3.3.2. *The strong-shock limit*

Analogous analysis can be carried out for the strong-shock limit. Substituting (3.9*a*–*d*) into the general solution of the first-order partial derivatives leads to the strong-shock

https://doi.org/10.1017/jfm.2020.775 Published online by Cambridge University Press

limits of (B 1)–(B 4) in appendix B, where M' is understood similarly as in (3.13*a*,*b*), such that, upon using (3.11), one has

$$M' = \frac{\mathrm{d}M}{\mathrm{d}x} = \frac{1}{a_0 M}\left(\frac{\partial M}{\partial t}\right)_\beta \sim -\zeta_1 \Phi M + \frac{\zeta_2 Q_1}{\rho_0 a_0^3 M^2}. \tag{3.17}$$

It is thus observed that $M' \sim O(M)$, so the M' notation is preferably kept in (B 1)–(B 4) and henceforth for convenient identification of the leading-order behaviour.

Again, substituting (3.9*a–d*), (B 1)–(B 4) and (3.17) into (3.14) yields the limiting Q_1 equation,

$$\left(\frac{\partial Q_1}{\partial t}\right)_\beta = \gamma_1 \rho_0 a_0^4 \Phi^2 M^4 + \gamma_2 a_0 M \Phi Q_1 + \frac{\gamma_3 Q_1^2}{\rho_0 a_0^2 M^2} + \gamma_4 Q_2 + O(M^3), \tag{3.18}$$

where $\gamma_{1,2,3,4}$ are coefficients listed in table 1 in appendix A. Setting $Q_2 = 0$, which otherwise is assumed as $Q_2 \sim O(M^4)$, (3.18) is joined with (3.5) and (3.11) to form the GGSD-1 equations in the strong-shock limit:

$$\left.\begin{aligned} \frac{\partial Z}{\partial t} &= \mathrm{i} a_0 M \frac{\partial Z}{\partial \beta}\left|\frac{\partial Z}{\partial \beta}\right|^{-1}, \\ \frac{\partial M}{\partial t} &= -\zeta_1 a_0 \Phi M^2 + \frac{\zeta_2 Q_1}{\rho_0 a_0^2 M}, \\ \frac{\partial Q_1}{\partial t} &= \gamma_1 \rho_0 a_0^4 \Phi^2 M^4 + \gamma_2 a_0 \Phi M Q_1 + \frac{\gamma_3 Q_1^2}{\rho_0 a_0^2 M^2}. \end{aligned}\right\} \tag{3.19}$$

3.4. *Second-order GGSD system: GGSD-2*

The second-order GGSD system can be similarly established by incorporating the evolution of Q_2, governed by (2.31), where $k = 1$ and $Q_3 = 0$:

$$\begin{aligned} \left(\frac{\partial Q_2}{\partial t}\right)_\beta = &-a_0 M \Phi \frac{\partial^2}{\partial t^2}\left(\frac{\rho a^2 u}{a+u}\right) - a_0 M\left[\frac{\partial^2}{\partial t^2}\left(\frac{1}{a+u}\right) Q_1 + 2\frac{\partial}{\partial t}\left(\frac{1}{a+u}\right) Q_2\right] \\ &- a_0 M \frac{\partial}{\partial t}\left(\frac{\partial(\rho a)}{\partial t}\frac{\partial u}{\partial x} - \frac{\partial(\rho a)}{\partial x}\frac{\partial u}{\partial t}\right) - \left(\frac{a_0 M}{a+u} - 1\right) Q_3. \end{aligned} \tag{3.20}$$

Again, without the Q_3 correction, the rest of (3.20) is fully determined because the second-order partial derivatives, $\{\mathcal{F}^{n,m}[\xi^*] : \xi^* \in \{\rho, u, p, a\},\ n+m=2\}$, only depends on M, Q_1, Q_2 and ultimately Z. To see this, the apparent dependence of $(A'/A)'$ in (2.29*b*) for quasi-1-D flow here becomes

$$\frac{\mathrm{d}}{\mathrm{d}x}\left(\frac{A'}{A}\right) = \frac{1}{a_0 M}\left(\frac{\partial \Phi}{\partial t}\right)_\beta, \tag{3.21}$$

which can be evaluated according to the definition of Φ, (3.8), after obtaining the partial derivatives, $Z_{\beta t}$ and $Z_{\beta\beta t}$, from differentiating (3.1) and its complex conjugate with respect

https://doi.org/10.1017/jfm.2020.775 Published online by Cambridge University Press

to β, once and twice, respectively. As a result, one defines $\Psi \equiv (A'/A)'$ and arrives at

$$\Psi = \Psi(Z, M) = -\Phi^2 - \frac{1}{A^4 M}\left[A^2 \frac{\partial^2 M}{\partial \beta^2} - \mathrm{Re}\left(\frac{\partial^2 Z}{\partial \beta^2}\frac{\partial Z^*}{\partial \beta}\right)\frac{\partial M}{\partial \beta}\right], \tag{3.22}$$

where $A = |\partial Z/\partial \beta|$. The explicit expansion of (3.20) is determined next in the weak- and strong-shock limits.

3.4.1. *The weak-shock limit*

In order to obtain the various second-order partial derivatives involved in (3.20), the shock local acceleration is also required. This is computed by differentiating (3.11) (recall $\epsilon = M - 1$) as follows:

$$\frac{\partial^2 \varepsilon_w}{\partial t^2} = \frac{1}{4\alpha_1 \rho_0^2 a_0^2}\left\{\varepsilon_w \frac{\partial Q_1}{\partial t} + Q_1 \frac{\partial \varepsilon_w}{\partial t} - 2\alpha_1 \rho_0^2 a_0^3\left[\Phi \frac{\partial \varepsilon_w}{\partial t} + a_0 \varepsilon_w (1 + \varepsilon_w)\Psi\right]\right\} \sim O(\varepsilon_w), \tag{3.23}$$

where $\partial Q_1/\partial t$, $\partial \varepsilon_w/\partial t$, Φ and Ψ are known due to (3.15), (3.11), (3.8) and (3.22).

With (3.10*a–d*), (B 1)–(B 4), (3.22) and (3.23) available, expressions for the required second-order partial derivatives of flow variables are Taylor-expanded around $\varepsilon_w = 0$, yielding the leading-order behaviour given in (B 5)–(B 8) of appendix B. We note that $Q_2 \sim O(1/\varepsilon_w)$ and recall (3.15). Finally, substituting (3.10*a–d*) and (B 5)–(B 8) into (3.20), while letting $Q_3 = 0$, produces the evolution equation for Q_2 as $\epsilon \to 0$, which is then joined to (3.5), (3.11) and (3.15) to form the following GGSD-2 system in the weak-shock limit:

$$\left.\begin{aligned}
\frac{\partial Z}{\partial t} &= \mathrm{i} a_0 M \frac{\partial Z}{\partial \beta}\left|\frac{\partial Z}{\partial \beta}\right|^{-1}, \\
\frac{\partial M}{\partial t} &= (M-1)\left(-\frac{a_0 \Phi}{2} + \frac{Q_1}{4\alpha_1 \rho_0 a_0^2}\right), \\
\frac{\partial Q_1}{\partial t} &= \frac{Q_1}{2}\left(\frac{Q_1}{\alpha_1 \rho_0 a_0^2} - a_0 \Phi\right) + (M-1)Q_2, \\
\frac{\partial Q_2}{\partial t} &= \frac{[(\gamma+1)Q_1 - 2\rho_0 a_0^3 \Phi]Q_2}{4\rho_0 a_0^2}.
\end{aligned}\right\} \tag{3.24}$$

3.4.2. *The strong-shock limit*

As an analogy to (3.23), the second time derivative $\partial^2 M/\partial t^2$ is prepared first,

$$\frac{\partial^2 M}{\partial t^2} = -\zeta_1 a_0 M\left(a_0 \Psi M^2 + 2\Phi \frac{\partial M}{\partial t}\right) + \frac{\zeta_2}{\rho_0 a_0^2 M^2}\left(M \frac{\partial Q_1}{\partial t} - Q_1 \frac{\partial M}{\partial t}\right), \tag{3.25}$$

where $\partial Q_1/\partial t$, $\partial M/\partial t$, Φ and Ψ are found in (3.18), (3.11), (3.8) and (3.22), respectively. However, here in the strong-shock limit, it is more convenient to further attain $M'' \equiv$

https://doi.org/10.1017/jfm.2020.775 Published online by Cambridge University Press

$\mathrm{d}(M')/\mathrm{d}x$, fully expanded using (3.13*a*,*b*), (3.11), (3.18) and (3.25) as

$$M'' = [(\zeta_1^2 + \gamma_1\zeta_2)\Phi^2 - \zeta_1\Psi]M + \frac{(\zeta_1+\gamma_2)\zeta_2\Phi Q_1}{\rho_0 a_0^3 M^2} + \frac{\zeta_2(\gamma_3 - 2\zeta_2)Q_1^2}{\rho_0^2 a_0^6 M^5} + \frac{\zeta_2\gamma_4 Q_2}{\rho_0 a_0^4 M^3}. \tag{3.26}$$

Consequently, $M'' \sim M' \sim O(M)$ is established.

Next, the second-order partial derivatives contributing to the expansion of $\partial Q_2/\partial t$ can be expressed in terms of M'', for the same reason that M' is preferred in (B 1)–(B 4). The explicit asymptotic formulae are reported in (B 5)–(B 8) in appendix B. After evaluating (3.20) using (B 5)–(B 8) in the strong-shock limit, the GGSD-2 equations follow:

$$\left.\begin{aligned}
\frac{\partial Z}{\partial t} &= \mathrm{i}a_0 M \frac{\partial Z}{\partial \beta}\left|\frac{\partial Z}{\partial \beta}\right|^{-1},\\
\frac{\partial M}{\partial t} &= -\zeta_1 a_0 \Phi M^2 + \frac{\zeta_2 Q_1}{\rho_0 a_0^2 M},\\
\frac{\partial Q_1}{\partial t} &= \gamma_1\rho_0 a_0^4\Phi^2 M^4 + \gamma_2 a_0\Phi M Q_1 + \frac{\gamma_3 Q_1^2}{\rho_0 a_0^2 M^2} + \gamma_4 Q_2,\\
\frac{\partial Q_2}{\partial t} &= \rho_0 a_0^5 M^5(\chi_1\Phi\Psi + \chi_2\Phi^3) - a_0^2 M^2(\chi_3\Psi + \chi_4\Phi^2)Q_1 - \frac{\chi_5\Phi Q_1^2}{\rho_0 a_0 M}\\
&\quad + \frac{\chi_6 Q_1^3}{\rho_0^2 a_0^4 M^4} + \frac{\chi_7 Q_1 Q_2}{\rho_0 a_0^2 M^2} + \chi_8 a_0\Phi M Q_2,
\end{aligned}\right\} \tag{3.27}$$

where $\chi_{1,2,\ldots,8}$ are again constant functions of γ listed in table 1 in appendix A. This completes the derivation of the shock-evolution equations used presently.

3.5. *Unbounded linear growth*

We now demonstrate that the zeroth-order GGSD system is linearly stable, whilst including the Q_1 correction in the first-order GGSD equations leads to linearized solutions that exhibit unbounded growth in time. Equations (3.16) and (3.19) are expanded around a plane shock of constant Mach number M_0, and consequently a steady downstream flow with $Q_1 = Q_{10}$. The plane shock motion is described by $Z_0 = \beta + \mathrm{i}a_0 M_0 t$, and the following rescaled perturbation fields are considered,

$$Z = Z_0 + z_1(\beta, t)\delta + \cdots, \quad M = M_0 + m_1(\beta, t)\delta + \cdots, \quad Q_1 = Q_{10} + q_1(\beta, t)\delta + \cdots, \tag{3.28a–c}$$

where $\delta \ll 1$ is the dimensionless perturbation size, and the subscript '1' is used to distinguish from unscaled variables used in (3.2*a*,*b*) and (3.6). The $\delta \to 0$ asymptotic behaviour is explored next for the limiting equations (3.16) and (3.19), corresponding to weak and strong shocks where the respective $M_0 \to 1$ and $M_0 \to \infty$ limits have been applied. Substituting (3.28*a–c*) into (3.16) and (3.19) yields, at order $O(\delta^0)$, that, for both weak and strong shocks,

$$Q_{10} = 0, \tag{3.29}$$

https://doi.org/10.1017/jfm.2020.775 Published online by Cambridge University Press

implying that the linear behaviour of the shock is fully described by the zeroth-order GGSD system. Further, at order $O(\delta)$, one has

$$\frac{\partial z_1}{\partial t} = \frac{\mathrm{i}a_0 M_0}{2}\left(\frac{\partial z}{\partial \beta} - \frac{\partial z^*}{\partial \beta}\right) + \mathrm{i}a_0 m_1, \tag{3.30a}$$

$$\frac{\partial m_1}{\partial t} = \begin{cases} \dfrac{\zeta_2 q_1}{\rho_0 a_0^2 M_0} - \dfrac{\mathrm{i}\zeta_1 a_0 M_0^2}{2}\left(\dfrac{\partial^2 z_1}{\partial \beta^2} - \dfrac{\partial^2 z_1^*}{\partial \beta^2}\right), & M_0 \to \infty, \\ \dfrac{(M_0-1)q_1}{4\alpha_1 \rho_0 a_0^2} - \dfrac{\mathrm{i}a_0(M_0-1)}{4}\left(\dfrac{\partial^2 z_1}{\partial \beta^2} - \dfrac{\partial^2 z_1^*}{\partial \beta^2}\right), & M_0 \to 1, \end{cases} \tag{3.30b}$$

$$\frac{\partial q_1}{\partial t} = 0. \tag{3.30c}$$

As a result of (3.30*c*), q_1 is a constant function of β to be determined from the initial conditions of the flow immediately behind the shock, namely,

$$q_1(\beta, t) = q_1(\beta, 0), \quad \forall\, t > 0. \tag{3.31}$$

By differentiating (3.30*a*) with respect to β, (3.30*b*) can be cast into

$$\frac{\partial m_1}{\partial t} = \begin{cases} -\dfrac{\zeta_1 M_0}{2}\dfrac{\partial}{\partial t}\left(\dfrac{\partial z_1}{\partial \beta} + \dfrac{\partial z_1^*}{\partial \beta}\right) + \dfrac{\zeta_2 q_1}{\rho_0 a_0^2 M_0}, & M_0 \to \infty, \\ -\dfrac{(M_0-1)}{4M_0}\dfrac{\partial}{\partial t}\left(\dfrac{\partial z_1}{\partial \beta} + \dfrac{\partial z_1^*}{\partial \beta}\right) + \dfrac{(M_0-1)q_1}{4\alpha_1 \rho_0 a_0^2}, & M_0 \to 1, \end{cases} \tag{3.32}$$

which can be integrated with respect to t because of (3.31) to give

$$m_1 = \begin{cases} -\dfrac{\zeta_1 M_0}{2}\left(\dfrac{\partial z_1}{\partial \beta} + \dfrac{\partial z_1^*}{\partial \beta}\right) + \dfrac{\zeta_2 q_1}{\rho_0 a_0^2 M_0} t + f(\beta), & M_0 \to \infty, \\ -\dfrac{M_0 - 1}{4}\left(\dfrac{\partial z_1}{\partial \beta} + \dfrac{\partial z_1^*}{\partial \beta}\right) + \dfrac{(M_0-1)q_1}{4\alpha \rho_0 a_0^2} t + f(\beta), & M_0 \to 1, \end{cases} \tag{3.33}$$

where $f(\beta)$ is prescribed from the initial Mach-number profile $m_1(\beta, 0)$. Further, (3.33) is substituted into (3.30*a*), to show

$$\frac{\partial z_1}{\partial \tau} = \begin{cases} \mathrm{i}\left(\dfrac{1-\zeta_1}{2}\dfrac{\partial z}{\partial \beta} - \dfrac{1+\zeta_1}{2}\dfrac{\partial z^*}{\partial \beta} + \dfrac{\zeta_2 q_1 \tau}{\rho_0 a_0^3 M_0^3} + \dfrac{f}{M_0}\right), & M_0 \to \infty, \\ \mathrm{i}\left(\dfrac{3-M_0}{4}\dfrac{\partial z_1}{\partial \beta} - \dfrac{1+M_0}{4}\dfrac{\partial z_1^*}{\partial \beta} + \dfrac{(M_0-1)q_1 \tau}{4\alpha_1 \rho_0 a_0^3} + f\right), & M_0 \to 1, \end{cases} \tag{3.34}$$

where $\tau = a_0 M_0 t$ is a time-like length unit defined for convenience. The solution for z_1 can be obtained using a Fourier expansion in β,

$$z_1(\beta, \tau) = \sum_{n=-\infty}^{\infty} \hat{z}_n(\tau)\, \mathrm{e}^{\mathrm{i}n\beta}, \quad q_1(\beta) = \sum_{n=-\infty}^{\infty} \hat{q}_n\, \mathrm{e}^{\mathrm{i}n\beta}, \quad f(\beta) = \sum_{n=-\infty}^{\infty} \hat{f}_n\, \mathrm{e}^{\mathrm{i}n\beta}, \tag{3.35a–c}$$

https://doi.org/10.1017/jfm.2020.775 Published online by Cambridge University Press

in both (3.34) and its complex conjugate. This yields the following second-order ordinary differential equations for the Fourier coefficients $\hat{z}_n$:

$$\frac{\mathrm{d}^2\hat{z}_n}{\mathrm{d}\tau^2} = \begin{cases} -\zeta_1 n^2\hat{z}_n + \mathrm{i}\left[\dfrac{\zeta_2(1-n\tau)\hat{q}_n}{\rho_0 a_0^3 M_0^3} - \dfrac{n\hat{f}_n}{M_0}\right], & M_0 \to \infty, \\ -\dfrac{M_0-1}{2}n^2\hat{z}_n + \mathrm{i}\left[\dfrac{(M_0-1)(1-n\tau)\hat{q}_n}{4\alpha_1\rho_0 a_0^3} - n\hat{f}_n\right], & M_0 \to 1, \end{cases} \tag{3.36}$$

whose solutions are given by

$$\hat{z}_n = \begin{cases} A_n\cos\left(\sqrt{\zeta_1}n\tau\right) + B_n\sin\left(\sqrt{\zeta_1}n\tau\right) + \mathrm{i}(C_n\tau + D_n), & M_0 \to \infty, \\ A_n\cos\left(\sqrt{\tfrac{1}{2}(M_0-1)}\,n\tau\right) + B_n\sin\left(\sqrt{\tfrac{1}{2}(M_0-1)}\,n\tau\right) + \mathrm{i}(C_n\tau + D_n), & M_0 \to 1, \end{cases} \tag{3.37}$$

where A_n and B_n are constants to be determined from the initial shock shape $z_1(\beta, 0)$, and from the particular linear source term,

$$C_n = \begin{cases} \dfrac{-\zeta_2\hat{q}_n}{\zeta_1\rho_0 a_0^3 M_0^3 n^2}, \\ \dfrac{-\hat{q}_n}{2\alpha_1\rho_0 a_0^3 n}, \end{cases} \qquad D_n = \begin{cases} \dfrac{\zeta_2\hat{q}_n - \rho_0 a_0^3 M_0^2 n\hat{f}_n}{\zeta_1\rho_0 a_0^3 M_0^3 n^2}, & M_0 \to \infty, \\ \dfrac{1}{2n^2}\left(\dfrac{\hat{q}_n}{\alpha_1\rho_1 a_0^3} - \dfrac{4n\hat{f}_n}{M_0-1}\right), & M_0 \to 1. \end{cases} \tag{3.38a,b}$$

Finally, substituting (3.38*a*,*b*) into (3.35*a*–*c*) and subsequently (3.33) completes the general solutions for z_1 and m_1.

If a shock is given an initial Mach-number perturbation, and the flow that produced the perturbation persists, a reasonable physical expectation could be that the shock develops a shape perturbation that grows linearly in the imaginary (shock-normal) direction with time. In the present theory, the forcing behind the shock is represented by the quantities Q_1 and Q_2. From (3.38*a*,*b*) and (3.33), for a flow with $Q_1 = 0$, where the shock is given an initial Mach-number perturbation and moves into a uniform medium, linear theory produces a solution that is the same as would be predicted by the linear zeroth-order GGSD (or GSD) model, where Q_1 plays no role. Here the shock motion consists of stable oscillations in the shock shape that are normal to its unperturbed profile, and with fixed amplitude and frequency.

For the present piston-generated shock, where the shock moves into a uniform medium but is subject to an initial perturbation with $Q_1 \neq 0$, linearized first-order GGSD predicts, in addition to oscillatory behaviour, a growth term that is linear in time for both the shock-shape and Mach-number perturbations, consistent with the above-stated expectation. Hence the linearized GGSD model suggests unbounded shock acceleration driven by non-uniformities (that is, non-zero Q_1) behind the shock. This amplitude growth, however, does not occur in alternative theories (e.g. Freeman 1957). In the sequel it will be shown that linear growth in time is in fact controlled by nonlinear behaviour.

4. Evolution of shock generated by a slightly corrugated piston

We now use the GGSD equations to investigate the evolution and nonlinear stability of a shock generated by an impulsively started piston of sinusoidal shape. The GGSD

https://doi.org/10.1017/jfm.2020.775 Published online by Cambridge University Press

approach is chosen over numerical solutions of the full Euler equations. Shock-capturing Euler methods contain their own shock modelling in the form of highly nonlinear artificial dissipation focused on the shock profile, making them a questionable choice for investigating the long-time evolution of tiny disturbances to a plane shock. A shock-fitting method would seem ideal but is difficult to implement at order sufficiently high to accurately capture spontaneous singularity formation.

4.1. *Base motion*

The shock considered in this study is produced by the impulsive motion of a piston from rest, whose velocity as a complex variable in the Y-direction is given by

$$U_p(t) = U\mathrm{H}(t)\,\mathrm{e}^{\mathrm{i}\pi/2}, \tag{4.1}$$

where $U > 0$ is the constant speed that the piston gains and $\mathrm{H}(t)$ is the Heaviside function. For a piston with flat surface located at $Y = 0$ moving into a uniform stationary medium, such an impulse in the limit of $U \to \infty$ or $U \to 0$ generates a normal plane shock of constant Mach number,

$$M_0 = \begin{cases} \dfrac{U}{\alpha_1 a_0}, & M \to \infty, \\ 1 + \dfrac{U}{2a_0\alpha_1}, & M \to 1, \end{cases} \tag{4.2}$$

after applying the strong- and weak-shock limits of the RH conditions (3.9*a–d*) and (3.10*a–d*). The base motion of the shock in the form of (3.2*a*,*b*) is thus established, namely,

$$Z_0 = \beta + \mathrm{i}a_0 M_0 t. \tag{4.3}$$

It is noted that, for $t > 0$, the shock-processed flow between the piston and shock front is uniform with velocity also given by (4.1). To proceed, non-dimensional variables are used according to a reference length scale L_0, such that $2\pi L_0$ is the initial perturbation wavelength; a reference velocity a_0 and density ρ_0. The time and pressure scales are thus derived as L_0/a_0 and $\rho_0 a_0^2$, respectively.

4.2. *Initial values for Z and M*

Next, a cosine perturbation of small amplitude $\epsilon \ll 1$ is imposed to the piston surface. Freeman (1955) showed that the corresponding shock generated by such a corrugated piston must have the same initial shape profile as the piston surface. Therefore, at $t = 0^+$, the shock shape is prescribed as

$$Z(\beta, 0^+) = Z_0(\beta, 0^+) + z(\beta, 0^+) = \beta + \mathrm{i}\epsilon\cos(\beta). \tag{4.4}$$

In order to obtain the initial Mach-number distribution of this curved shock produced by the same piston impulse (4.1), it is noted that, along the infinitely thin layer of fluid sandwiched between the piston and shock at $t = 0^+$, only the piston velocity component locally normal to the boundary is transferred into the fluid, whereas the tangential component slips through the fluid under the present Euler description. Therefore, in the laboratory frame where the piston velocity (4.1) is measured, the initial boundary fluid

https://doi.org/10.1017/jfm.2020.775 Published online by Cambridge University Press

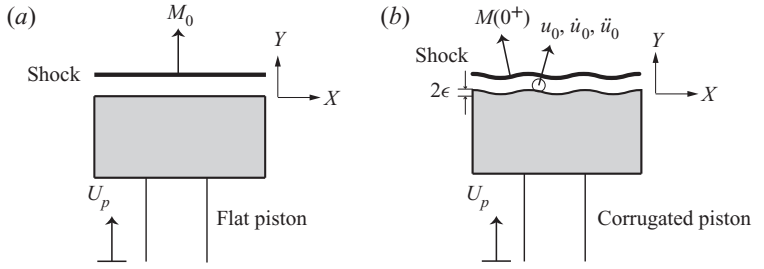


FIGURE 2. Shock generated by (*a*) a flat piston and (*b*) a corrugated piston of perturbation amplitude ϵ, at time $t = 0^+$. Both pistons share the same velocity U_p, giving a constant Mach number M_0 when the piston is flat. In (*b*) the Mach-number profile is $M(\beta, 0^+)$. The flow between the piston and the shock is uniform in (*a*), but non-uniform with initial velocity u_0, acceleration $\dot{u}_0$ and jerk $\ddot{u}_0$ in (*b*).

velocity distribution follows as the projection of piston velocity onto the unit normal vector given in (3.3), leading to

$$u_0 \equiv u(\beta, 0^+) = \begin{cases} \dfrac{\alpha_1 M_0}{\sqrt{\epsilon^2 \sin^2(\beta) + 1}}, & M_0 \to \infty, \\ \dfrac{2\alpha_1 (M_0 - 1)}{\sqrt{\epsilon^2 \sin^2(\beta) + 1}}, & M_0 \to 1, \end{cases} \tag{4.5}$$

where the base motion Mach number M_0 found in (4.2) is used as the input parameter. Because the shock curve coincides with the piston surface at $t = 0^+$, the normal RH conditions can be applied again to convert (4.5) into the required initial values of Mach number,

$$M(\beta, 0^+) = \begin{cases} \dfrac{M_0}{\sqrt{\epsilon^2 \sin^2(\beta) + 1}}, & M_0 \to \infty, \\ 1 + \dfrac{M_0 - 1}{\sqrt{\epsilon^2 \sin^2(\beta) + 1}}, & M_0 \to 1. \end{cases} \tag{4.6}$$

A schematic comparison between shocks generated by flat and corrugated pistons is shown in figure 2, where the infinitesimal layer of shock-processed flow attached to the piston boundary at $t = 0^+$ is illustrated with kinematic quantities including acceleration and jerk that are discussed in the next section.

4.3. *Initial values for Q_1 and Q_2*

To complete the GGSD initial value problem formulation for the piston-generated shock, it remains to determine Q_1 and Q_2 at $t = 0^+$. This is achieved by utilizing two kinematic conditions of the boundary flow, about its initial acceleration $\dot{u}_0$ and jerk $\ddot{u}_0$ in the shock-normal direction. For each β, these quantities take the form of a full derivative moving with the piston,

$$\dot{u}_0(\beta) = u_t(\beta, 0^+) + u_0 u_x(\beta, 0^+), \tag{4.7a}$$

$$\ddot{u}_0(\beta) = \left.\frac{\partial (u_t + u u_x)}{\partial t}\right|_{t=0^+} + u_0 \left.\frac{\partial (u_t + u u_x)}{\partial x}\right|_{t=0^+}, \tag{4.7b}$$

https://doi.org/10.1017/jfm.2020.775 Published online by Cambridge University Press

where u_0 is derived in (4.5), and the first- and second-order derivatives of u are given in (B 1)–(B 4) and (B 5)–(B 8), respectively, in appendix B.

Expanding (4.7*a*) using (B 2*a*) and (B 2*b*), while in the strong-shock case expressing M' in terms of Q_1 via (3.17), leads to the initial values for Q_1,

$$Q_1(\beta, 0^+) = \begin{cases} \dfrac{M(\beta,0^+)^2}{\zeta_2}\left[\zeta_1\Phi M + \dfrac{4\gamma M(u_0-1)\Phi + (\gamma+1)^2\dot{u}_0}{2(\gamma+1)(4M-3u_0)}\right]_{t=0^+}, & M_0 \to \infty, \\ \left.\dfrac{4(M-1)\Phi(-2\gamma+(3\gamma-1)u_0+2)+2(\gamma+1)^2\dot{u}_0}{(\gamma+1)^2(2M-u_0-1)}\right|_{t=0^+}, & M_0 \to 1, \end{cases} \tag{4.8}$$

where, in both limits, $\Phi|_{t=0^+}$ can be evaluated from its definition (3.8) using the initial shock profile (4.4) as

$$\Phi(\beta, 0^+) = \frac{\epsilon\cos(\beta)}{(\epsilon^2\sin^2(\beta)+1)^{3/2}}. \tag{4.9}$$

Substituting (4.5), (4.6) and (4.9) into (4.8) completes the expression. Specifically, evaluating $Q_1(\beta, 0^+)$ at $\epsilon = 0$ shows that

$$Q_1(\beta, 0^+)|_{\epsilon=0} = \begin{cases} \dfrac{(\gamma+1)M_0\dot{u}_0(\beta)}{(8-6\alpha_1)\zeta_2}, & M_0 \to \infty, \\ \dfrac{2\dot{u}_0(\beta)}{1-2(\alpha_1-1)(M_0-1)}, & M_0 \to 1. \end{cases} \tag{4.10}$$

As discussed in § 4.1, the unperturbed flow between the piston and shock is uniform, implying that $Q_1(\beta, 0^+)|_{\epsilon=0} = 0$ for all β. Therefore, it is concluded that $\dot{u}_0(\beta) = 0$, that is, the initial boundary flow is acceleration-free. Hence $Q_1(\beta, 0^+)$ simplifies to yield the following leading-order behaviour as $\epsilon \to 0$:

$$Q_1(\beta, 0^+) \sim \begin{cases} \dfrac{M_0^3\epsilon\cos(\beta)[\alpha_1(3(\gamma+1)\zeta_1-2\gamma)-4(\gamma+1)\zeta_1]}{(3\alpha_1-4)(\gamma+1)\zeta_2}, & M_0 \to \infty, \\ \dfrac{8(M_0-1)\epsilon(1-\gamma)\cos(\beta)}{(\gamma+1)^2}, & M_0 \to 1. \end{cases} \tag{4.11}$$

We note that our conclusion that the initial boundary flow along the piston surface has zero acceleration, with consequence (4.11), does not involve truncation error associated with the GGSD systems. Instead, the presence of the Q_1 correction in the evolution equation of M allows its initial condition to be inferred without knowledge of higher-order corrections $Q_{i\geq 2}$.

Next, expanding (4.7*b*) in terms of u_t, u_x, u_{tt}, u_{tx} and u_{xx} evaluated at $t = 0^+$ produces a linear equation from which the initial value of Q_2 can be solved. With a similar derivation provided in appendix C, it is shown again that the initial flow attached to the piston boundary has to be jerk-free, i.e. $\ddot{u}_0 = 0$, in order to recover the unperturbed uniform result.

https://doi.org/10.1017/jfm.2020.775 Published online by Cambridge University Press

Thus in appendix C, the asymptotic form of $Q_2(\beta, 0^+)$ for small ϵ follows,

$$Q_2(\beta, 0^+) \sim \begin{cases} (\xi_1 \cos^2(\beta) + \xi_2 \sin^2(\beta)) M_0^4 \epsilon^2, & M_0 \to \infty, \\ -\dfrac{32\gamma \cos^2(\beta)(M_0 - 1)^3 \epsilon^2}{(\gamma + 1)^3}, & M_0 \to 1, \end{cases} \tag{4.12}$$

where ξ_1 and ξ_2 are coefficient functions of γ tabulated in table 2 in appendix A.

With initial conditions served by (4.4), (4.6), (4.11) and (4.12), evolution of the shock generated by the perturbed piston can be tracked by the GGSD systems up to second order, by integrating in time the system of equations (3.24) and (3.27) for weak and strong shocks, respectively. While, at $t = 0$, the initial values for M, Q_1 and Q_2 can be obtained faithfully from the full 2-D Euler equations, the GGSD construction does not directly propagate additional flow disturbances due to the piston motion, and carried by the C^+ characteristics when $t > 0$. Our adoption of the GGSD theory therefore assumes that perturbations caused by the corrugated piston after the initial impulse are small and smooth; while, sufficiently far from the piston wall, the shock dynamics is mainly controlled by the intrinsic nonlinearity of its free propagation. The question of whether shock motion predicted by the GGSD systems as a function of time converge to the true solution for the Euler equations when the GGSD system order increases remains open until a direct comparison can be made.

5. Numerical results

We describe numerical simulations of the initial value problem formulated in § 4 for the specific heat ratio fixed at $\gamma = 5/3$. Spatial derivatives with respect to β in the GGSD systems are discretized using a fourth-order compact finite-difference scheme (Lele 1992), for its ability to capture travelling waves and pseudo-spectral convergence, on a uniform grid in β of size $N = 2048$. The spectral method is not used owing to large aliasing errors produced to the high-order nonlinearities in the systems. Time integration is performed with a variable time-stepping fourth-order Runge–Kutta method (RK4). All results are presented using the length unit $\tau = a_0 M_0 t$ for time measurement, as τ corresponds to the distance travelled by an unperturbed shock at any given time t.

If the shock profile remains smooth, we expect that $M(\beta, t)$ and $z(\beta, t)$ will remain single-valued functions with bounded derivatives. We consider that a singularity has appeared at a time when an unbounded derivative in any quantity, of any order, has developed. As the systems evolve, an edge-detection algorithm (Gelb & Tadmor 2006) that searches for discontinuities on discrete data is applied on the dataset representing $M(\beta, t)$. A brief outline of the algorithm is given in appendix D. Detection of an 'edge' in the discrete $M(\beta, t)$ at some $t = t_c$ is interpreted to indicate the presence of an infinite $\partial M/\partial\beta$ corresponding to 'overturning,' and hence a singularity in the GGSD solution. This will generally also indicate the occurrence of curvature singularities in the shock shape Z (Mostert *et al.* 2017, 2018*a*). For each set of given initial values, varying the choices of the two required tuning parameters q and J_{crit} (see (D 7) and (D 8) in appendix D) leads to less than 2 % variations in estimating t_c compared to the reported t_c values obtained using $q = 1.1$ and $J_{crit} = 1$.

For $t > t_c$, the numerical solution for $M(\beta, t)$ quickly develops rapid oscillations around the jump location. The spatial derivatives, $\partial M/\partial\beta$ and $\partial^2 M/\partial\beta^2$, can no longer be accurately captured by the compact finite-difference method. Proper continuation of the shock evolution for $t > t_c$ would require the insertion of a shock–shock into the GGSD

https://doi.org/10.1017/jfm.2020.775 Published online by Cambridge University Press

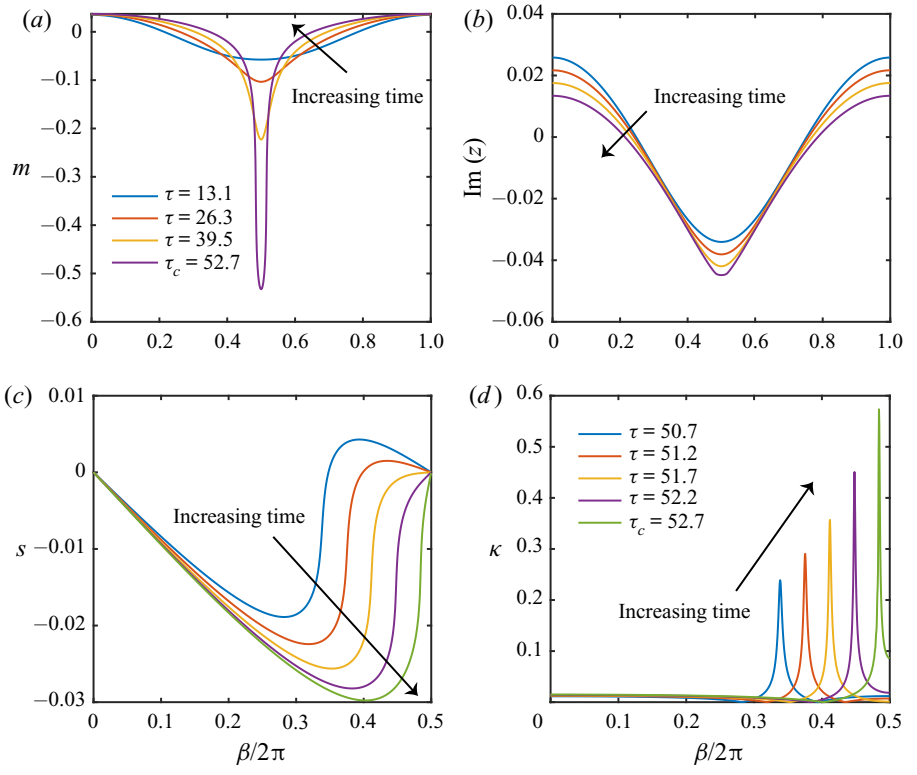


FIGURE 3. Spontaneous development of curvature singularities illustrated using GGSD-0 with initial conditions $M_0 = 50$ and $\epsilon = 0.03$. The Mach-number and shock-shape perturbation profiles are given over four oscillation periods up to the critical time in (*a*) and (*b*), respectively. The shock slope and curvature distributions are shown as the critical time is approached with time increments of $\Delta\tau = 0.5$ in (*c*) and (*d*), respectively.

shock-evolution description, much as is done following shock formation for the Euler equations (Eggers *et al.* 2017). Our present interest is evolution up to $t = t_c$ only, and so this is not done presently. It is demonstrated subsequently that all three GGSD systems, the zeroth, first and second order, predict spontaneous development of curvature singularities on the shock shape at a finite time that is inversely proportional to the small initial perturbation size ϵ. The critical time at which singularity occurs converges within the GGSD hierarchy as the order of systems increases.

5.1. *Spontaneous singularity formation*

We first show the perturbation profiles of Mach number m and shock shape z as a function of the ray-tube marker β in figure 3(*a*) and (*b*), respectively, for successive times obtained using GGSD-0 with initial piston Mach number $M_0 = 50$ and perturbation amplitude $\epsilon = 0.03$. Here, curves of different times are separated by the period of the fundamental linear mode in (3.37), i.e. $\Delta\tau = 1/\sqrt{\zeta_1} = 13.2$, up to the critical time, $t_c = 52.7$, when discontinuities in m are detected by the edge-detection algorithm. As time increases, it is seen in figure 3(*a*) that the symmetric m distribution steepens in each oscillation cycle, and correspondingly in figure 3(*b*) the normal shock displacement given by $\mathrm{Im}(z)$ evolves towards the formation of two kinks. Because the lateral displacement $\mathrm{Re}(z)$ is a

https://doi.org/10.1017/jfm.2020.775 Published online by Cambridge University Press

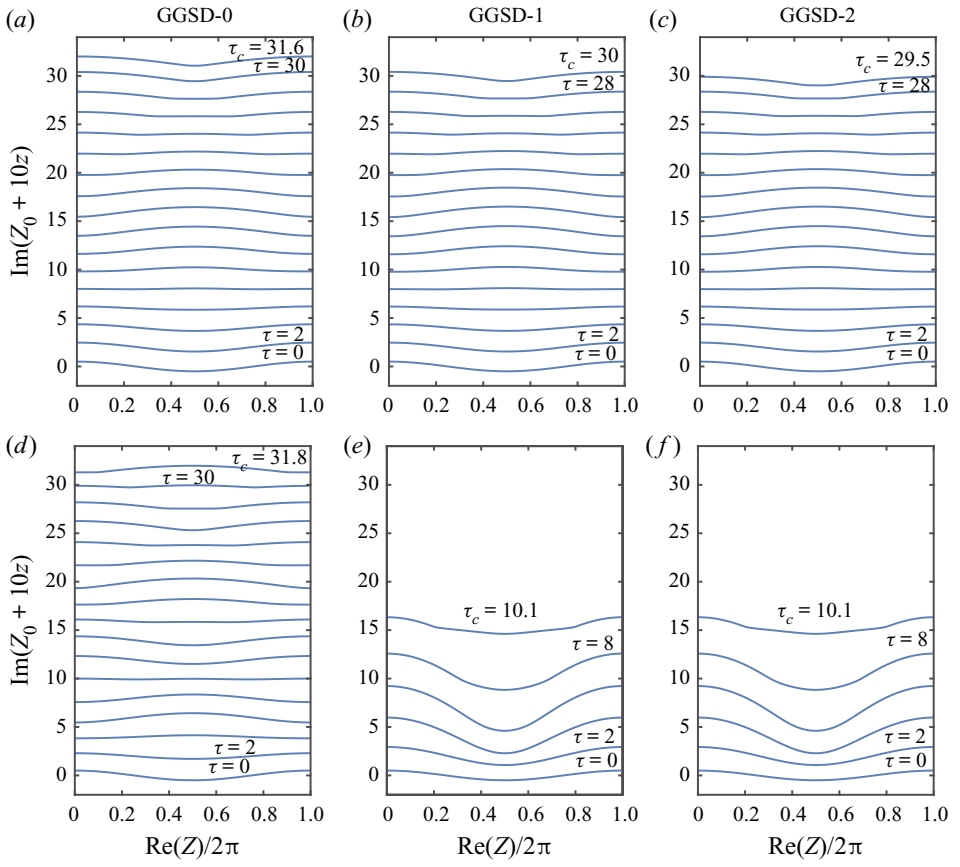


FIGURE 4. Shock trajectories with perturbation in the Y-direction amplified 10 times for piston perturbation size $\epsilon = 0.05$. The initial piston Mach number is $M_0 = 1.1$ in (*a–c*) and $M_0 = 10$ in (*d–f*), corresponding to results obtained from the zeroth-, first- and second-order GGSD systems, respectively. In each panel, successive trajectories are shown in increments of $\Delta\tau = 2$, up to the final curve given at the critical time τ_c.

continuous function of β, the observed loss of continuity in m and smoothness in z also occur spatially in terms of shock positions Z. In a closer look, figure 3(*c*) and (*d*) employ a smaller time interval $\Delta\tau = 0.5$ within one period for the same parameters $M_0 = 50$ and $\epsilon = 0.03$ to show, leading up to the critical time, the evolution of shock slope s, calculated as $s = \mathrm{Im}(\partial Z/\partial\beta)/\mathrm{Re}(\partial Z/\partial\beta)$, and curvature κ, identified as $\kappa = \Phi$ thanks to (2.22) and (3.13*a*,*b*). We see that, near the critical time, s is everywhere finite but approaching a discontinuity at the point where κ appears to form a singularity. These results are consistent with the findings of Mostert *et al.* (2018*a*), where the Whitham's original GSD equations are applied to a hypothetical initial value problem for a plane shock with a single Mach-number perturbation.

Although the example given here is obtained using GGSD-0, the character of the spontaneous curvature singularity development is similarly found for GGSD-1 and GGSD-2. It is thus suggested that the 'shock–shock' mechanism described by Whitham (2011), where nonlinear compression waves propagating along the shock, reinforcing each other to the formation of discontinuities, also holds in the present study, where a global

https://doi.org/10.1017/jfm.2020.775 Published online by Cambridge University Press

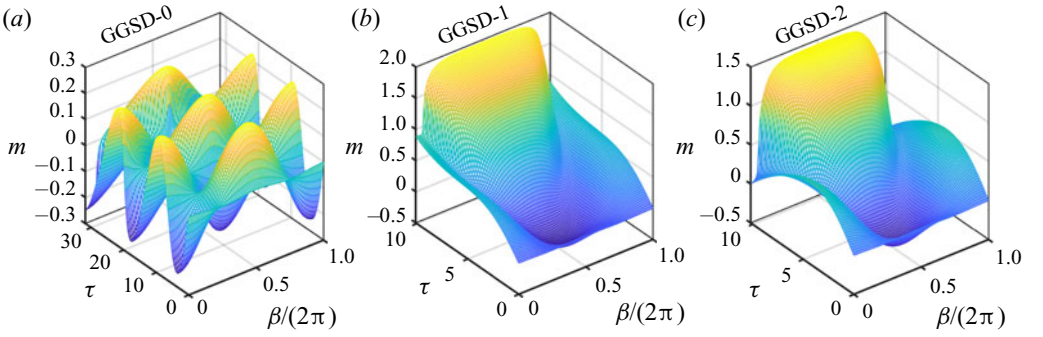


FIGURE 5. History of Mach-number perturbation profile m along the evolving shock, for $\epsilon = 0.05$ and $M_0 = 10$. Results obtained using three different orders of GGSD models are shown in (a)–(c).

A–M relation breaks down and non-uniform effects of the flow immediately behind the shock are accommodated.

Next, typical evolving trajectories of the weak and strong shocks for $0 \leq \tau \leq \tau_c$ predicated by the three GGSD systems are presented in figure 4 for both a weak shock with $M_0 = 1.1$, $\epsilon = 0.05$ (figure 4*a–c*) and a strong shock with $M_0 = 10$, $\epsilon = 0.05$ (figure 4*d–f*). A transition of the amplified shock shape from its smooth initial value to a non-differentiable profile with two cusps at the critical time is observed in all cases shown. The oscillatory shock-shape pattern given by GGSD-0 is evident in both limits, with oscillation frequencies that match the linear analysis of the fundamental mode in (3.37), i.e. $\omega = \sqrt{\zeta_1}$ in the strong-shock limit ($M_0 = 10$) and $\omega = \sqrt{(M_0 - 1)/2}$ in the weak-shock limit ($M_0 = 1.1$). Comparing the GGSD models of different orders, differences in the detailed trajectories are small for $M_0 = 1.1$, noting that the values for τ_c are also close to each other. This suggests that, in the weak-shock limit, the non-uniform effect behind the shock is small and that GGSD-0 provides a good approximation.

In contrast, with $M_0 = 10$, the first- and second-order systems predict very similar trajectories with almost the same τ_c that is significantly shorter than the zeroth-order value. In this case, evolution of the Mach-number perturbation m is further investigated in figure 5 using the same parameters $M_0 = 10$ and $\epsilon = 0.05$, where the profiles of m along the shock are shown for the entire history of the shock trajectories. The nonlinear solution of GGSD-0 seen in figure 5(a) again shows the oscillatory pattern that is consistent with the corresponding linear theory, noting that stable oscillation in time is here terminated by the onset of discontinuities in m owing to reinforcing waves on the shock. In contrast, for GGSD-1 and GGSD-2, where linear analysis predicts a growth that is linear in time, the Mach-number profiles in figure 5(b) and (c) demonstrate that the underlying osculations are dominated by approximately linear growth, until nonlinear effects accumulate, leading to m discontinuities at the critical time. This result shows that the initial and subsequent downstream non-uniformity plays a crucial role in determining the shock motion.

5.2. *Critical time*

Figure 6 shows τ_c given by the three GGSD systems as a function of the piston perturbation ϵ, in both strong-shock (figure 6*a*,*b*) and weak-shock (figure 6*c*,*d*) limits. First, in agreement with the observation made from figure 4, the strong-shock limit sees a dramatic

https://doi.org/10.1017/jfm.2020.775 Published online by Cambridge University Press

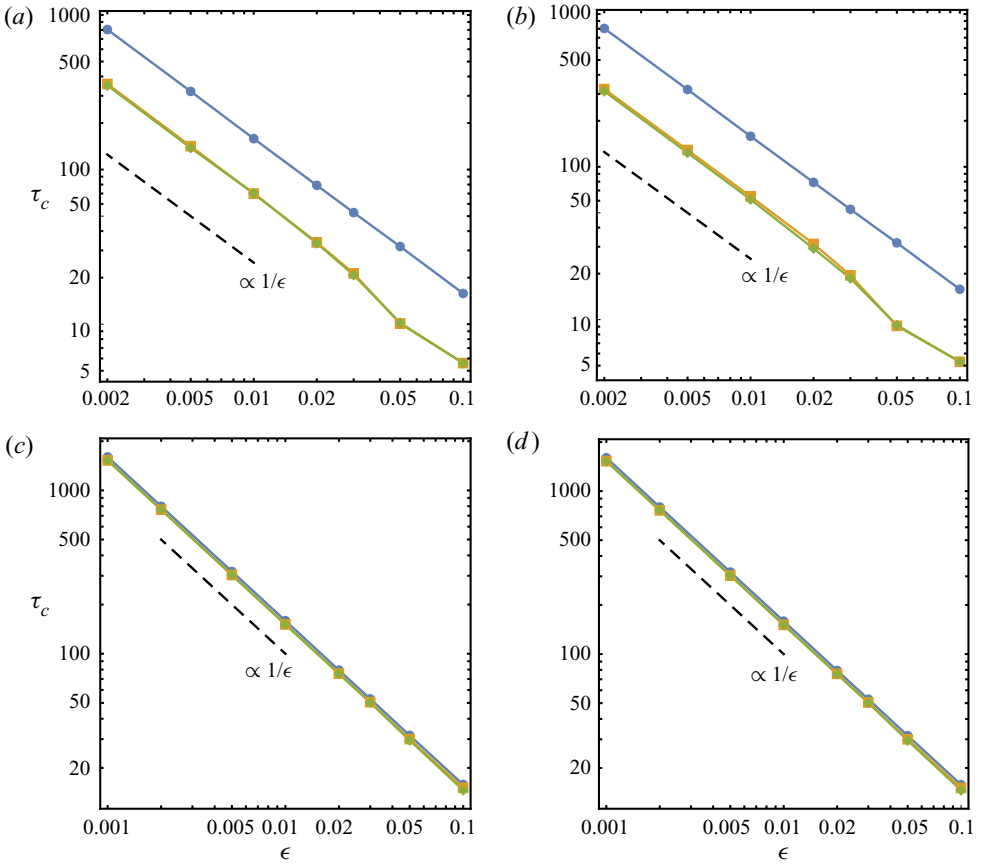


FIGURE 6. Critical times in strong- and weak-shock limits given for (*a*) $M_0 = 10$, (*b*) $M_0 = 50$, (*c*) $M_0 = 1.1$ and (*d*) $M_0 = 1.02$. In all four cases, results obtained using GGSD-0 are shown as circles, GGSD-1 as squares and GGSD-2 as diamonds. In each panel, the dashed line without markers displays a reference function that has inverse power law of degree one.

reduction in τ_c comparing GGSD-0 to the other two higher-order models, while GGSD-1 and GGSD-2 appear to have converged within the GGSD framework in terms of their τ_c predictions. The weak-shock limit shows much smaller differences between the three models. When at least the Q_1 correction is considered in the equations, for the cases shown here with initial Mach numbers $M_0 = 10$ and $M_0 = 50$, the decrease in τ_c is found to be over 50 % across all simulations with varying ϵ. For $M_0 = 1.1$ and $M_0 = 1.02$, a decrease in τ_c is still consistently present, although the magnitude falls within the uncertainties of the edge-detection algorithm. On the other hand, the difference made by further including the Q_2 correction in GGSD-2 is insignificant for all M_0 simulated. These results provide convincing evidence for the convergence of the GGSD hierarchy and showcase the power of higher-order methods in handling shocks that lead to a strongly non-uniform flow, whose effect seems to increase with Mach number.

An intuitive explanation of the GGSD hierarchy convergence in this application can be offered by comparing the order-of-magnitude estimates made for Q_1 and Q_2 when deriving the GGSD equations, to the independently calculated initial values of Q_1 and Q_2. In §§ 3.2 and 3.3, it was shown that $Q_1 \gtrsim O(\varepsilon_w^0)$ and $Q_2 \gtrsim O(1/\varepsilon_w)$ as $\varepsilon_w = M - 1 \to 0$,

https://doi.org/10.1017/jfm.2020.775 Published online by Cambridge University Press

and $Q_1 \gtrsim O(M^3)$ and $Q_2 \gtrsim O(M^4)$ as $M \to \infty$, in order to retain the corresponding Q_1 and Q_2 corrections in the leading-order dominant balance. Meanwhile, as $\epsilon \to 0$, the initial conditions for Q_1 and Q_2, obtained in § 4.3 without the GGSD truncation error, are $Q_1 \sim \epsilon(M_0 - 1)$ and $Q_2 \sim \epsilon^2(M_0 - 1)^3$ as $M_0 \to 1$, and $Q_1 \sim \epsilon M_0^3$ and $Q_2 \sim \epsilon^2 M_0^4$ as $M_0 \to \infty$. As a result, the initial condition that best matches its minimum order of magnitude required by the asymptotic GGSD equations is that of Q_1 in the strong-shock limit, where indeed the effect of Q_1 on τ_c is shown to be the largest.

Another finding of interest from figure 6 is that all three GGSD methods show a critical time $\tau_c(\epsilon)$ as inversely proportional to the initial perturbation size ϵ for sufficiently small ϵ, for all Mach numbers M_0. A suggested form is

$$\tau_c = \tau_c(\epsilon, M_0; d) = \frac{K_1(M_0; d)}{\epsilon}, \quad \epsilon \ll 1, \tag{5.1}$$

where K_1 is a proportionality constant that depends on M_0 and the order of the GGSD models, $d \in \{0, 1, 2\}$. The asymptotic domain of minimum ϵ where (5.1) applies seems to be M_0-dependent, particularly for strong shocks. Together with the similar analytic form obtained by Mostert *et al.* (2018*a*), the present results, including the established connection between the GGSD hierarchy and the Euler equations, provides compelling evidence that (5.1) is a universal form for perturbed planar shock waves.

From a computational perspective, we note that, in figure 6, the smallest ϵ achieved in the strong-shock limit is $\epsilon = 0.002$, doubling the value $\epsilon = 0.001$ in the weak-shock limit. This is because an explicit time integration method such as RK4 appears to be unstable and costly for further reduction in ϵ. An implicit method might be preferred should results for $\epsilon < 0.002$ and $M \gg 1$ be desired. This is not done presently owing to the associated high cost of iteratively solving order-N nonlinear equations at each time step.

To illustrate that the choice of M_0 in figure 6 adequately represents the strong- and weak-shock limits, figure 7 plots τ_c for two sequences of extreme values of M_0, obtained for $\epsilon = 0.02$ when $M_0 \gg 1$ and for $\epsilon = 0.01$ when $M_0 - 1 \ll 1$, in all three GGSD systems. Convergence in τ_c is clear as $M_0 > 50$ and $M_0 - 1 < 0.02$ for strong and weak shocks, respectively.

5.3. *Diagnostic statistics*

We have seen in figure 4 that the GGSD-1 and GGSD-2 in the strong-shock limit produce distinctly interesting shock trajectories before curvature singularities form. Figure 8 therefore presents the key statistics that characterize the evolution given by these higher-order methods up to their critical times using $M_0 = 50$ and $\epsilon = 0.02$. The mean and standard deviation of Mach-number perturbation over the shock, defined as

$$\bar{m} = \frac{1}{2\pi}\int_0^{2\pi} m \,\mathrm{d}\beta \quad \text{and} \quad \sigma(m) = \left(\frac{1}{2\pi}\int_0^{2\pi} (m - \bar{m}) \,\mathrm{d}\beta\right)^{1/2}, \tag{5.2a,b}$$

are shown in figure 8(*a*) and (*b*), respectively. It is observed that GGSD-0 gives an oscillating Mach-number perturbation profile around the mean, which is zero, across the profile, for all time until a discontinuity develops (critical time not shown for the dot-dashed lines in figure 8). GGSD-1 and GGSD-2 both produce on average an upward drift for m over time, where the increase is smaller with GGSD-2. This is consistent with the linear analysis in § 3.5, where (3.33) and (3.38*a*,*b*) clearly state the linear growth. Whether this mean drift will further reduce with increasing order of the GGSD

https://doi.org/10.1017/jfm.2020.775 Published online by Cambridge University Press

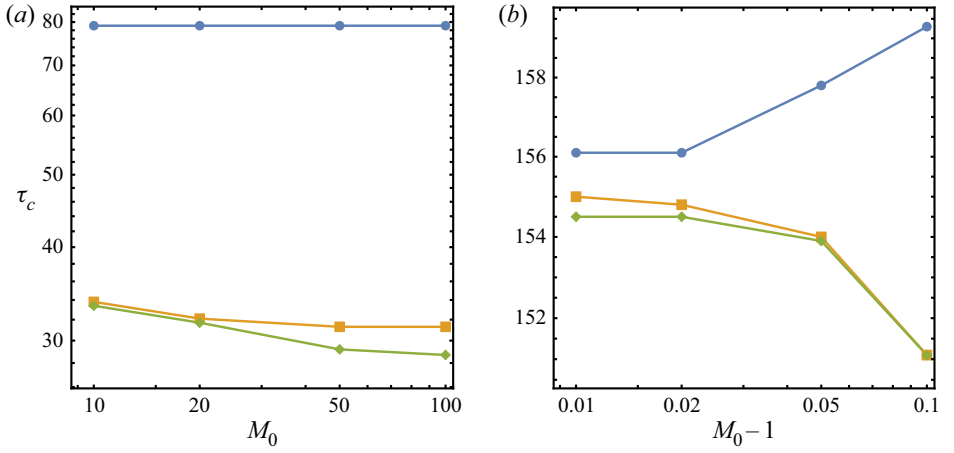


FIGURE 7. Convergence of critical time (a) as M_0 increases in the strong-shock limit for $\epsilon = 0.02$, and (b) as M_0 decreases in the weak-shock limit for $\epsilon = 0.01$. Circles, squares and diamonds correspond to GGSD-0, GGSD-1 and GGSD-2 data, respectively.

systems, or if it faithfully represents the Euler equations, remains to be confirmed by direct comparisons against direct numerical simulations of the full Euler equations with high-order-accurate shock tracking. Nevertheless, despite the mean rise, the standard deviation of m obtained from GGSD-1 and GGSD-2 shows qualitatively similar periodic fluctuations that do not grow in times, as seen in GGSD-0.

Further, as a consequence of the positive Mach-number perturbation increasing, the shock trajectories given by the higher-order methods must be accelerating at an increasingly faster rate compared to either the unperturbed flat shock or the GGSD-0 prediction. Indeed, this is reflected in figure 8(c) where the mean shock advancement, $\mathrm{Im}(\bar{Z})$, is plotted as a function of τ. As expected from $\bar{m} = 0$, the zeroth-order GGSD system yields a history of mean shock positions that is exactly the same as the unperturbed shock; whereas with an increasing positive $\bar{m}$, the mean shock position given by GGSD-1 and GGSD-2 accelerates and outruns the flat shock. Particularly, the Q_2 correction made by GGSD-2 to GGSD-1 partially negates the Q_1 correction applied by GGSD-1 to GGSD-0. Additionally, figure 8(d) shows that, although the standard deviation $\sigma(|z|)$, defined analogously to (5.2a,b), is significantly larger in GGSD-1 and GGSD-2 compared to GGSD-0, the shock-shape perturbations remain bounded.

The negation effect of GGSD-2 is related to the measure of immediate non-uniformity Q_1 shown in figure 9, as a function of the evolving shock position in the complex plane for the same parameters $M_0 = 50$ and $\epsilon = 0.02$. Identically zero in GGSD-0, the evolution of non-zero Q_1 in the higher-order models has been demonstrated to provide a considerable Mach-number correction. Specifically, comparing figure 9(a) and figure 9(b), the overall larger increase of Q_1 given by GGSD-1 than GGSD-2, especially the fact that when the critical time is approached Q_1 actually decreases in GGSD-2, matches the different growth rates of $\bar{m}$ observed in figure 8(a).

Curiously, with reference to figure 8(b), the distance gap between the mean shock positions predicted by GGSD-1 and GGSD-2 is further examined in figure 10. Denoting ΔY as the lead distance, its maximum obviously occurs at the critical time of each model. The percentage of $\max(\Delta Y)$ over the advancement of the reference flat shock, which

https://doi.org/10.1017/jfm.2020.775 Published online by Cambridge University Press

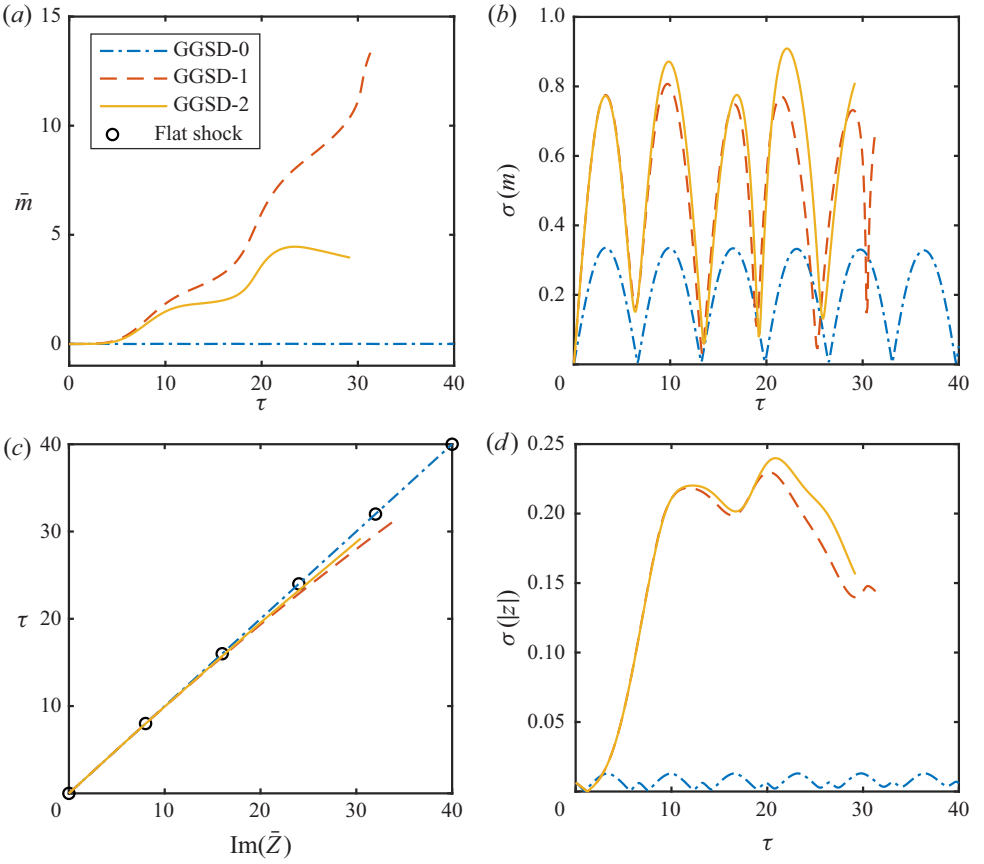


FIGURE 8. Temporal shock-profile statistics comparison between the flat (hollow circles) and perturbed shock due to three GGSD systems (different lines), made for $M_0 = 50$ and $\epsilon = 0.02$. (*a*,*b*) Mean and standard deviation of the Mach-number perturbation profile. (*c*) Average shock advancement in the unperturbed shock-normal direction. (*d*) Standard deviation of the shock-shape perturbation.

also equals τ_c by definition, is shown in figure 10(*a*) as a function of ϵ. A converging result of approximately 9.5 % for GGSD-1 and 4.5 % for GGSD-2 is found, noting that $\max(\Delta Y)/\tau_c$ is overall weakly dependent on the simulated range of ϵ. More interestingly, examining ΔY at a given time τ that is at most the earliest critical time among different models, i.e. $\tau < \min_{d\in\{0,1,2\}}(\tau_c(M_0; d))$, for instance choosing $\tau = \tau_c(0.03, 50; 2) = 18.6$ as shown in figure 10(*b*), reveals a quadratic scaling law with respect to ϵ, which holds for both GGSD-1 and GGSD-2, that is,

$$\Delta Y|_\tau = K_2(M_0; d)\epsilon^2, \tag{5.3}$$

where again K_2 is the constant multiplier that depends on M_0 and order number $d \in \{1, 2\}$.

In order to enable such distance lead obtained using higher-order methods over a flat shock, the flow behind the shock must gain more kinetic energy from the corrugated piston advancing than for the flat piston flow. Unlike a flat piston whose motion is given by the Heaviside function (see (4.1)), which advances at the same speed with the flow behind the

https://doi.org/10.1017/jfm.2020.775 Published online by Cambridge University Press

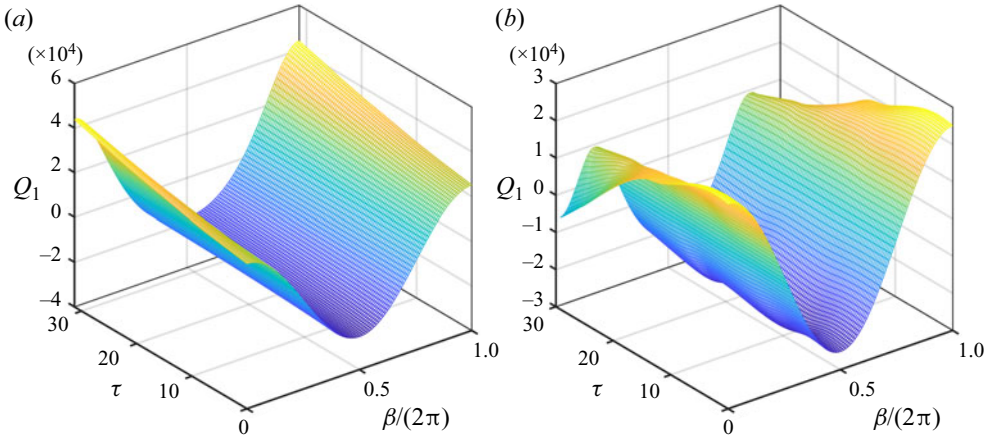


FIGURE 9. History of the non-uniformity measure Q_1 behind the evolving shock as a function of shock positions in two dimensions. The panels compare results obtained for $M_0 = 50$ and $\epsilon = 0.02$, using (*a*) GGSD-1 and (*b*) GGSD-2.

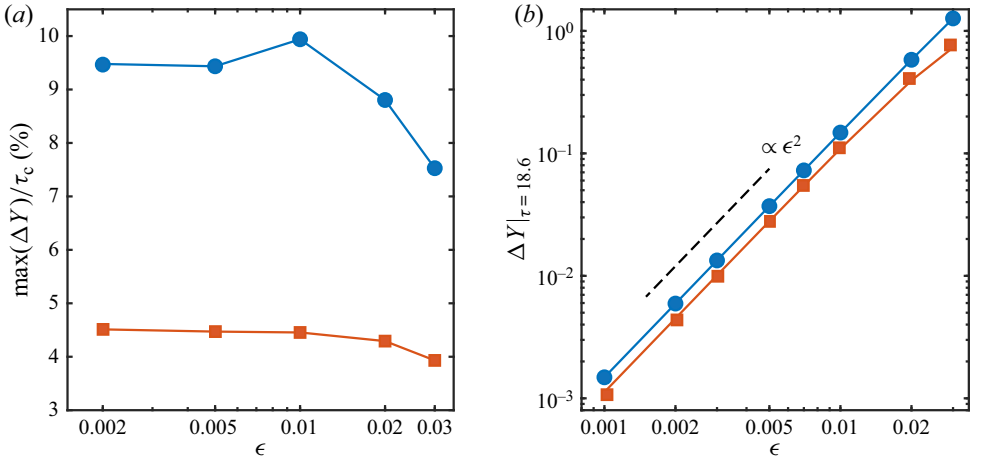


FIGURE 10. (*a*) Percentage maximum distance lead of average shock position given by GGSD-1 (circles) and GGSD-2 (squares) over the reference flat shock. (*b*) Distance lead of average shock position at a fixed time that is the critical time for the second-order method. In both cases, $M_0 = 50$ and $\epsilon = 0.03$, and the dashed line represents the first-order result, while the solid line gives the second-order method. The dashed line without markers in (*b*) shows an explicit function of quadratic power law.

shock for all $t > 0$, a corrugated piston of the same velocity continues to accelerate fluid in the local normal direction, possibly generating more kinetic energy into the flow for $t > 0$.

6. Conclusions

We have reported numerical simulations of the evolution of a shock produced by an impulsively accelerated, two-dimensional piston with a sinusoidal surface corrugation

https://doi.org/10.1017/jfm.2020.775 Published online by Cambridge University Press

of amplitude ϵ. First a complex-variable formulation of generalized geometrical shock dynamics, referred to as GGSD, is derived up to second order for both strong- and weak-shock limits. The resulting closed systems of partial differential equations are then solved numerically to give the evolution of the shock-shape and Mach-number distributions. An edge-detection algorithm is applied to test for the appearance of a singularity in the shock evolution profile at some critical time τ_c. These simulations provide strong evidence supporting the hypothesis that a spontaneous curvature singularity develops in the shock shape as a prelude to the formation of triple points or Mach stems in τ_c inversely proportional to the amplitude of the piston corrugation.

The adoption of the GGSD hierarchy overcomes the limitations of previously used theories of geometrical shock dynamics, first by accommodating well-defined shock initial conditions for the shock generation process, which are calculated exactly for the piston-driven shock according to the Euler equations, and second by incorporating a quantitative description of non-uniform flow effects immediately behind the shock. The behaviour of weak shocks with Mach number close to unity is found to witness small changes when increasing the system order, while maintaining oscillations around the unperturbed shock up to the critical time of curvature singularity formation. For strong shocks with large Mach number, the inclusion of non-uniform flow correction $Q_1 \neq 0$ behind the shock in GGSD-1 and GGSD-2 predicts an overall shock acceleration compared to GGSD-0 where $Q_1 = 0$. The corresponding Mach-number perturbation growth is eventually terminated by the onset of the curvature singularity, which occurs in GGSD-1 and GGSD-2 at τ_c that converges with the GGSD order increasing, and that scales as $\tau_c \propto 1/\epsilon$ as in GGSD-0, albeit with a significantly smaller proportionality constant. Between the higher-order methods, GGSD-2 gives a smaller Q_1 correction effect than GGSD-1, manifested particularly in the smaller average shock acceleration relative to the unperturbed shock. This leaves uncertainty in the convergence of shock trajectories given by the GGSD expansion hierarchy, and remains to be resolved by direct numerical simulations for the Euler equations with accurate shock tracking.

Acknowledgements

This work was supported by the KAUST Office of Sponsored Research under Award No. URF/1/3418-01. The authors also thank Professor H. G. Hornung for helpful discussions.

Declaration of interests

The authors report no conflict of interest.

Appendix A. Tables of coefficients

This section lists all the coefficient functions used throughout this study in tables 1 and 2, as constant functions of the specific heat ratio γ.

Appendix B. Partial derivatives of flow variables

The partial derivatives used in the expansions of GGSD systems are given in this section. Asymptotic expressions of the general solutions to (2.28) are obtained for both the weak- and strong-shock limits up to second order.

https://doi.org/10.1017/jfm.2020.775 Published online by Cambridge University Press

$$\bar{\mu} = \sqrt{\frac{\gamma-1}{2\gamma}}$$

$$\alpha_1 = \frac{2}{\gamma+1}$$

$$\alpha_2 = \frac{\gamma+1}{\gamma-1}$$

$$\alpha_3 = \frac{2\gamma\bar{\mu}}{\gamma+1}$$

$$\sigma_1 = \frac{4\gamma(\gamma(2(5\gamma-7)+3\gamma(4\gamma-5)\bar{\mu}+\bar{\mu})+4)}{(\gamma-1)^2(\gamma+1)(\gamma\bar{\mu}+1)^2} - \frac{4\sqrt{2\gamma}(\gamma^2+\gamma+2)}{(\gamma-1)^{3/2}(\gamma+1)^2}$$

$$\sigma_2 = \frac{\gamma^2(\gamma(\gamma(\gamma(3\gamma-10)-4)-2)+2(\gamma((\gamma-17)\gamma-9)+5)\bar{\mu}-3)}{(\gamma-1)(\gamma+1)^3(\gamma\bar{\mu}+1)^3}$$

$$\sigma_3 = \frac{4\gamma^2(4\gamma+(\gamma(5\gamma-2)-1)\bar{\mu}-2)}{(\gamma-1)(\gamma+1)^2(\gamma\bar{\mu}+1)^2}$$

$$\sigma_4 = \frac{2\sqrt{2\gamma}}{(\gamma-1)^{3/2}(\gamma+1)^3}\left(\gamma(-\gamma^2+\gamma-15) + \frac{\gamma(\gamma+1)(\gamma(\gamma(7\gamma-18)+(\gamma(\gamma+1)(7\gamma-15)+10)\bar{\mu}-11)+24)}{(\gamma\bar{\mu}+1)^3} + 3\right)$$

$$\sigma_5 = \frac{8(\gamma(2\gamma-11)+10)}{(\gamma^2-1)^2\bar{\mu}} - \frac{\sqrt{2}\gamma^{3/2}(3\gamma^4\bar{\mu}+\gamma^3(9-33\bar{\mu})+17\gamma^2(5\bar{\mu}-3)+\gamma(91-103\bar{\mu})-73)}{(\gamma-1)^{5/2}(\gamma+1)(\gamma\bar{\mu}+1)^3}$$

$$\sigma_6 = -\frac{(1+\gamma)^2}{4(1+\bar{\mu}\gamma)^2}\left(\frac{4(7\gamma-6)}{\gamma^2-1} + \frac{2\sqrt{2}(\gamma(5\gamma-12)+9)\sqrt{\gamma}}{(\gamma-1)^{3/2}(\gamma+1)}\right)$$

$$\sigma_7 = \frac{\gamma(9(\gamma-1)\gamma+(3\gamma((\gamma-1)\gamma+3)+11)\bar{\mu}-9)+5}{4\bar{\mu}(\gamma+1)(\gamma\bar{\mu}+1)^3}$$

$$\sigma_8 = -\frac{\gamma((2\gamma-1)\bar{\mu}+3)}{(\gamma\bar{\mu}+1)^2}$$

$$\sigma_9 = \frac{\sqrt{\gamma}(\gamma(\gamma(23\gamma-54)+13)+2(\gamma(\gamma(\gamma(4\gamma-11)+17)-5)-2)\bar{\mu}+20)}{\sqrt{2}(\gamma-1)^{3/2}(\gamma\bar{\mu}+1)^3}$$

$$\sigma_{10} = \frac{\sqrt{\gamma}(\gamma+1)(\gamma(\gamma(75\gamma-253)+233)+(\gamma(\gamma(\gamma(29\gamma-111)+191)-173)+88)\bar{\mu}-31)}{2\sqrt{2}(\gamma-1)^{5/2}(\gamma\bar{\mu}+1)^3}$$

$$\sigma_{11} = -\frac{4\sqrt{2\gamma}(\gamma(2\gamma-11)+11)}{(\gamma-1)^{5/2}(\gamma+1)}$$

$$\sigma_{12} = \frac{8\gamma(5\gamma+1)\bar{\mu}}{(\gamma^2-1)^2}$$

$$\sigma_{13} = \frac{2\sqrt{2\gamma}(5\gamma((\gamma-3)\gamma-1)+39)}{(\gamma-1)^{7/2}(\gamma+1)}$$

$$\sigma_{14} = \frac{(\gamma+1)(6\gamma^2\bar{\mu}+\gamma(8-10\bar{\mu})-8)}{(\gamma-1)(2\gamma\bar{\mu}+2)^2}$$

$$\sigma_{15} = \frac{\gamma(2(\gamma-1)\bar{\mu}+4)}{(2\gamma\bar{\mu}+2)^2}$$

$$\zeta_1 = \frac{(\gamma-1)\gamma}{\gamma+\gamma^2(2\bar{\mu}+1)-2}$$

$$\zeta_2 = \frac{(\gamma-1)(\gamma+1)(\gamma(2\bar{\mu}-1)+1)}{4(\gamma+\gamma^2(2\bar{\mu}+1)-2)}$$

$$\gamma_1 = -\frac{4(\gamma-2)\gamma^2((\gamma-1)^2+(\gamma^3-\gamma^2-2)\bar{\mu})}{(\gamma+1)(\gamma\bar{\mu}+1)^2(\gamma+\gamma^2(2\bar{\mu}+1)-2)^2}$$

$$\gamma_2 = -\frac{\gamma(\gamma^4+\gamma^3(54\bar{\mu}-47)+8\gamma^2(3\bar{\mu}+4)-4\gamma(2\bar{\mu}+7)+32)}{(\gamma-2)^4(\gamma+1)}$$

$$\gamma_3 = \frac{(\gamma+1)(4\gamma+\gamma^4(13\bar{\mu}-9)+\gamma^3(51-68\bar{\mu})+\gamma^2(52\bar{\mu}-54)+8)}{2(\gamma-2)^4}$$

$$\gamma_4 = \frac{\gamma-\gamma\bar{\mu}-1}{\gamma-2}$$

$$\chi_1 = \zeta_1(\sigma_1+\sigma_{12}-\sigma_{11}\zeta_1)-\sigma_3$$

TABLE 1. For caption see next page.

https://doi.org/10.1017/jfm.2020.775 Published online by Cambridge University Press

$$\chi_2 = \zeta_1(\sigma_4 + \sigma_{11}\gamma_1\zeta_2) - \sigma_1\gamma_1\zeta_2 - (\sigma_1 + \sigma_5)\zeta_1^2 + (\sigma_{11} + \sigma_{13})\zeta_1^3 - \sigma_2$$

$$\chi_3 = -\zeta_1(\sigma_6 + \sigma_{11}\zeta_2) + \sigma_{12}\zeta_2 + \sigma_8$$

$$\chi_4 = \sigma_7 - \sigma_9\zeta_1 + (\sigma_1 - 2\sigma_5 - \sigma_{11}\gamma_2)\zeta_1\zeta_2 + (\sigma_6 + \sigma_{10} + 3\sigma_{13}\zeta_2)\zeta_1^2 + (\sigma_4 + \sigma_6\gamma_1 + \sigma_1\gamma_2 + \sigma_{11}\gamma_1\zeta_2)\zeta_2$$

$$\chi_5 = \zeta_2(\sigma_9 + \sigma_1\gamma_3 - 2\sigma_{10}\zeta_1 - \sigma_{11}\gamma_3\zeta_1 + \sigma_6(\gamma_2 + \zeta_1) + \zeta_2(-2\sigma_1 + \sigma_5 + \sigma_{11}\gamma_2 + 3\sigma_{11}\zeta_1 - 3\sigma_{13}\zeta_1))$$

$$\chi_6 = \zeta_2(-\sigma_6\gamma_3 - (\sigma_{10} - 2\sigma_6 + \sigma_{11}\gamma_3)\zeta_2 + (2\sigma_{11} - \sigma_{13})\zeta_2^2)$$

$$\chi_7 = \zeta_2(-\sigma_6\gamma_4 + 2\sigma_{14} - \sigma_{11}\gamma_4\zeta_2)$$

$$\chi_8 = 2(\sigma_{15} - \sigma_{14}\zeta_1) + \gamma_4\zeta_2(\sigma_{11}\zeta_1 - \sigma_1)$$

TABLE 1 (cntd). Constant coefficient functions in the GGSD systems, up to second order, in terms of the specific heat ratio γ.

$$\omega_1 = \frac{8(5\gamma-2)}{\gamma^2-1}, \quad \omega_2 = -\frac{8\gamma(2\gamma^2+3\gamma-1)}{(\gamma-1)(\gamma+1)^3}, \quad \omega_3 = \frac{8\gamma(2\gamma-1)}{(\gamma-1)(\gamma+1)^2}, \quad \omega_4 = \frac{8(\gamma-3)\gamma}{(\gamma-1)(\gamma+1)^2}$$

$$\omega_5 = -\frac{8(\gamma-4)\gamma}{(\gamma-1)^2(\gamma+1)}, \quad \omega_6 = \frac{8-28\gamma}{\gamma^2-1}, \quad \omega_7 = \frac{4\gamma(3\gamma^2+6\gamma-1)}{(\gamma-1)(\gamma+1)^3}, \quad \omega_8 = \frac{4(1-3\gamma)\gamma}{(\gamma-1)(\gamma+1)^2}$$

$$\omega_9 = \frac{4\gamma(\gamma+3)}{(\gamma-1)(\gamma+1)^2}, \quad \omega_{10} = \frac{8(4\gamma^2-9\gamma+2)}{(\gamma-1)^2(\gamma+1)}, \quad \omega_{11} = \frac{4(7\gamma-6)}{\gamma^2-1}, \quad \omega_{12} = -\frac{4\gamma(3\gamma+5)}{(\gamma+1)^3}$$

$$\omega_{13} = \frac{12\gamma}{(\gamma+1)^2}, \quad \omega_{14} = -\frac{4(\gamma^2+3\gamma-2)}{(\gamma-1)(\gamma+1)^2}, \quad \omega_{15} = -\frac{8(4\gamma-3)}{\gamma^2-1}, \quad \omega_{16} = -\frac{4(5\gamma-4)}{\gamma^2-1}$$

$$\omega_{17} = \frac{8\gamma(\gamma+2)}{(\gamma+1)^3}, \quad \omega_{18} = -\frac{8\gamma}{(\gamma+1)^2}, \quad \omega_{19} = \frac{4(3\gamma-2)}{\gamma^2-1}, \quad \omega_{20} = \frac{8(5\gamma-4)}{\gamma^2-1}$$

$$\omega_{21} = \frac{4(\gamma+1)(5\gamma-7)}{(\gamma-1)^3}, \quad \omega_{22} = -\frac{4(3\gamma^2+5\gamma-2)}{(\gamma-1)^2(\gamma+1)}, \quad \omega_{23} = \frac{8\gamma-4}{(\gamma-1)^2}, \quad \omega_{24} = -\frac{4(5\gamma^2+8\gamma-15)}{(\gamma-1)^3}$$

$$\omega_{25} = -\frac{4(10\gamma^3+\gamma^2-22\gamma-13)}{(\gamma-1)^4}, \quad \omega_{26} = -\frac{2(\gamma+1)(7\gamma-11)}{(\gamma-1)^3}, \quad \omega_{27} = \frac{2(5\gamma^2+10\gamma-3)}{(\gamma-1)^2(\gamma+1)}, \quad \omega_{28} = \frac{2-6\gamma}{(\gamma-1)^2}$$

$$\omega_{29} = \frac{22\gamma^2+28\gamma-58}{(\gamma-1)^3}, \quad \omega_{30} = \frac{4(10\gamma^3+\gamma^2-22\gamma-13)}{(\gamma-1)^4}, \quad \omega_{31} = -\frac{2\sqrt{2}(5\gamma^2-12\gamma+9)}{\left(\frac{\gamma-1}{\gamma}\right)^{3/2}\gamma(\gamma+1)}$$

$$\omega_{32} = \frac{\sqrt{2}(5\gamma^3+\gamma^2-17\gamma+7)}{\sqrt{\frac{\gamma-1}{\gamma}}(\gamma+1)^3}, \quad \omega_{33} = -\frac{2\sqrt{2-\frac{2}{\gamma}}\gamma(2\gamma-1)}{(\gamma+1)^2}, \quad \omega_{34} = \frac{4\sqrt{2}(\gamma^3-13\gamma+13)}{\left(\frac{\gamma-1}{\gamma}\right)^{3/2}\gamma(\gamma+1)^2}$$

$$\omega_{35} = \frac{\sqrt{2}(11\gamma^3-33\gamma^2-15\gamma+61)}{\left(\frac{\gamma-1}{\gamma}\right)^{5/2}\gamma^2(\gamma+1)}, \quad \omega_{36} = \frac{\sqrt{2}(-7\gamma^2+16\gamma-13)}{\left(\frac{\gamma-1}{\gamma}\right)^{3/2}\gamma(\gamma+1)}, \quad \omega_{37} = \frac{2\sqrt{2}(2\gamma^3+\gamma^2-8\gamma+3)}{\sqrt{\frac{\gamma-1}{\gamma}}(\gamma+1)^3}$$

$$\omega_{38} = -\frac{\sqrt{2-\frac{2}{\gamma}}\gamma(3\gamma-1)}{(\gamma+1)^2}, \quad \omega_{39} = \frac{2\sqrt{2}(3\gamma^3-3\gamma^2-23\gamma+25)}{\left(\frac{\gamma-1}{\gamma}\right)^{3/2}\gamma(\gamma+1)^2}, \quad \omega_{40} = \frac{2\sqrt{2}(7\gamma^2-29\gamma+28)}{\left(\frac{\gamma-1}{\gamma}\right)^{5/2}\gamma^2}$$

$$\omega_{41} = \frac{2(7\gamma-5)}{\gamma^2-1}, \quad \omega_{42} = -\frac{4\gamma(\gamma+3)}{(\gamma+1)^3}, \quad \omega_{43} = \frac{4\gamma}{(\gamma+1)^2}, \quad \omega_{44} = \frac{8-16\gamma^2}{(\gamma-1)(\gamma+1)^2}, \quad \omega_{45} = -\frac{8(5\gamma-4)}{\gamma^2-1}$$

$$\nu_1 = \frac{8}{\gamma+1}$$

$$\nu_2 = \frac{4\gamma}{(\gamma+1)2}$$

$$\nu_3 = \frac{6}{\gamma+1}$$

$$\iota_1 = \omega_{14} - \nu_1\nu_2 - 2\omega_{15}\zeta_1 + 2\nu_1\nu_3\zeta_1 + \omega_{11}(\gamma_2 + \zeta_1)$$

TABLE 2. For caption see next page.

https://doi.org/10.1017/jfm.2020.775 Published online by Cambridge University Press

$$\iota_2 = \omega_{44} - 2\omega_{45}\zeta_1 + \omega_{41}(\gamma_2 + \zeta_1)$$
$$\iota_3 = 2(\omega_{19} + \nu_2\nu_3 - (2\omega_{20} + \nu_3^2)\zeta_1 + \omega_{16}(\gamma_2 + \zeta_1))$$
$$\iota_4 = \omega_{41}(\gamma_3 - 2\zeta_2) + \omega_{45}\zeta_2$$
$$\iota_5 = -\omega_{11}\gamma_3 + 2\omega_{11}\zeta_2 - \omega_{15}\zeta_2 + \nu_1\nu_3\zeta_2$$
$$\iota_6 = 2\omega_{16}(\gamma_3 - 2\zeta_2) + (2\omega_{20} + \nu_3^2)\zeta_2$$
$$\iota_7 = 2(\omega_{16}\gamma_1\zeta_2 + \omega_{17} + \omega_{18} - \omega_{19}\zeta_1 - \nu_2\nu_3\zeta_1) + \nu_2^2 + (2(\omega_{16} + \omega_{20}) + \nu_3^2)\zeta_1^2$$
$$\iota_8 = \omega_{18} - \omega_{16}\zeta_1$$
$$\iota_9 = \omega_{12} + \omega_{13} + \zeta_1(\nu_1\nu_2 - \omega_{14} + (\omega_{11} + \omega_{15} - \nu_1\nu_3)\zeta_1) + \omega_{11}\gamma_1\zeta_2$$
$$\iota_{10} = \omega_{13} - \omega_{11}\zeta_1$$
$$\iota_{11} = \omega_{42} + \omega_{43} - \omega_{44}\zeta_1 + (\omega_{41} + \omega_{45})\zeta_1^2 + \omega_{41}\gamma_1\zeta_2$$
$$\iota_{12} = \omega_{43} - \omega_{41}\zeta_1$$
$$\lambda_1 = \alpha_1(\alpha_1\iota_{11} + \iota_7)$$
$$\lambda_2 = \tfrac{\nu_1\zeta_1 + \alpha_1(\nu_2 - \nu_3\zeta_1)}{(\nu_1 - \alpha_1\nu_3)^2\zeta_2}$$
$$\lambda_3 = (\alpha_1(\alpha_1\iota_4 + \iota_6) - \iota_5)(\nu_1\zeta_1 + \alpha_1(\nu_2 - \nu_3\zeta_1))$$
$$\lambda_4 = (\alpha_1(\alpha_1\iota_2 + \iota_3) + \iota_1)(\nu_1 - \alpha_1\nu_3)\zeta_2$$
$$\xi_1 = -\tfrac{\lambda_1 + \iota_9 + \lambda_2(\lambda_3 + \lambda_4)}{(\omega_{11} + \alpha_1(2\omega_{16} + \omega_{41}\alpha_1))\gamma_4\zeta_2}$$
$$\xi_2 = \tfrac{2\alpha_1\iota_8 + \iota_{10} + \alpha_1^2\iota_{12}}{\gamma_4\zeta_2(\omega_{11} + 2\alpha_1\omega_16 + \alpha_1^2\omega_{41})}$$

TABLE 2 (cntd). Constant coefficients for the second-order partial derivatives of flow variables in the strong-shock limit, found in (B 5)–(B 8), and those for the initial value of Q_2, found in (C 1), associated with a shock driven by a corrugated piston. These coefficients are expressed in terms of other constant functions of γ listed in table 1.

In the weak-shock limit where $\varepsilon_w = M - 1 \to 0$, and in the strong-shock limit where $M \sim M' \to \infty$, the first-order partial derivatives are given by

$$\rho_t = \begin{cases} \dfrac{Q_1}{2a_0^2} + 2\left[\dfrac{2Q_1}{(1+\gamma)a_0^2} + \dfrac{(\gamma-3)\rho_0 a_0 \Phi}{(1+\gamma)^2}\right]\varepsilon_w + O(\varepsilon_w^2), & \varepsilon_w \to 0, \\ \rho_0 a_0\left[\dfrac{6(\gamma+1)}{(\gamma-1)^2}M' + \dfrac{2}{\gamma-1}\Phi M\right] + O(M^0), & M \to \infty, \end{cases} \tag{B 1a}$$

$$\rho_x = \begin{cases} \dfrac{-Q_1}{2a_0^3} + \left[\dfrac{(\gamma-3)Q_1}{(1+\gamma)a_0^3} - \dfrac{4(\gamma-1)\rho_0\Phi}{(1+\gamma)^2}\right]\varepsilon_w + O(\varepsilon_w^2), & \varepsilon_w \to 0, \\ -\rho_0\left[\dfrac{6(\gamma+1)}{(\gamma-1)^2}\dfrac{M'}{M} + \dfrac{2}{\gamma-1}\Phi\right] + O(M^{-1}), & M \to \infty, \end{cases} \tag{B 1b}$$

$$u_t = \begin{cases} \dfrac{Q_1}{2\rho_0 a_0} + \left[\dfrac{Q_1}{\rho_0 a_0} + \dfrac{4(\gamma-1)a_0^2\Phi}{(1+\gamma)^2}\right]\varepsilon_w + O(\varepsilon_w^2), & \varepsilon_w \to 0, \\ a_0^2 M\left[\dfrac{8}{\gamma+1}M' + \dfrac{4\gamma}{(\gamma+1)^2}\Phi M\right] + O(M^1), & M \to \infty, \end{cases} \tag{B 2a}$$

https://doi.org/10.1017/jfm.2020.775 Published online by Cambridge University Press

$$u_x = \begin{cases} \dfrac{-Q_1}{2\rho_0 a_0^2} + \left[\dfrac{(2-6\gamma)a_0\Phi}{(1+\gamma)^2}\right]\varepsilon_w + O(\varepsilon_w^2), & \varepsilon_w \to 0, \\ -a_0\left[\dfrac{6}{\gamma+1}M' + \dfrac{4\gamma}{(\gamma+1)^2}\Phi M\right] + O(M^0), & M \to \infty, \end{cases} \tag{B 2b}$$

$$p_t = \begin{cases} \dfrac{Q_1}{2} + 2\left[Q_1 + \dfrac{(\gamma-3)\rho_0 a_0^3\Phi}{(1+\gamma)^2}\right]\varepsilon_w + O(\varepsilon_w^2), & \varepsilon_w \to 0, \\ \rho_0 a_0^3 M^2\left[\dfrac{4(3\gamma-2)}{\gamma^2-1}M' + \dfrac{4\gamma}{(\gamma+1)^2}\Phi M\right] + O(M^2), & M \to \infty, \end{cases} \tag{B 3a}$$

$$p_x = \begin{cases} \dfrac{-Q_1}{2a_0} - \left[\dfrac{Q_1}{a_0} + \dfrac{4(\gamma-1)\rho_0 a_0^2\Phi}{(1+\gamma)^2}\right]\varepsilon_w + O(\varepsilon_w^2), & \varepsilon_w \to 0, \\ -4\rho_0 a_0^2 M\left[\dfrac{2\gamma-1}{\gamma^2-1}M' + \dfrac{\gamma}{(\gamma+1)^2}\Phi M\right] + O(M^1), & M \to \infty, \end{cases} \tag{B 3b}$$

and

$$a_t = \begin{cases} \dfrac{(\gamma-1)Q_1}{4\rho_0 a_0} + \left[\dfrac{(\gamma-1)Q_1}{2\rho_0 a_0} + \dfrac{(\gamma-1)(\gamma-3)a_0^2\Phi}{(1+\gamma)^2}\right]\varepsilon_w + O(\varepsilon_w^2), & \varepsilon_w \to 0, \\ 2a_0^2 M\sqrt{\dfrac{\gamma-1}{2\gamma}}\left[\dfrac{\gamma(3\gamma-5)}{\gamma^2-1}M' + \dfrac{\gamma(\gamma-1)}{(\gamma+1)^2}\Phi M\right] + O(M^1), & M \to \infty, \end{cases} \tag{B 4a}$$

$$a_x = \begin{cases} \dfrac{-(\gamma-1)Q_1}{4\rho_0 a_0^2} - \left[\dfrac{2(\gamma-1)^2 a_0\Phi}{(1+\gamma)^2}\right]\varepsilon_w + O(\varepsilon_w^2), & \varepsilon_w \to 0, \\ -a_0\sqrt{\dfrac{\gamma-1}{2\gamma}}\left[\dfrac{4\gamma(\gamma-2)}{\gamma^2-1}M' + \dfrac{2\gamma(\gamma-1)}{(\gamma+1)^2}\Phi M\right] + O(M^0), & M \to \infty. \end{cases} \tag{B 4b}$$

Similarly the limiting second-order partial derivatives as $\varepsilon_w \to 0$ and $M \sim M' \sim M'' \to \infty$ are as follows:

$$p_{tt} = \begin{cases} \dfrac{Q_2}{2} + O(\varepsilon_w^0), \\ \rho_0 a_0^4 M^2[M(\omega_1 M'' + (\omega_2+\omega_3)\Phi^2 M + \omega_3\Psi M) + \omega_4\Phi MM' + \omega_5 M'^2] + O(M^3), \end{cases} \tag{B 5a}$$

$$p_{tx} = \begin{cases} -\dfrac{Q_2}{2a_0} + O(\varepsilon_w^0), \\ \rho_0 a_0^3 M[M(\omega_6 M'' + (\omega_7+\omega_8)\Phi^2 M + \omega_8\Psi M) + \omega_9\Phi MM' + \omega_{10}M'^2] + O(M^2), \end{cases} \tag{B 5b}$$

$$u_{tt} = \begin{cases} \dfrac{Q_2}{2\rho_0 a_0} + O(\varepsilon_w^0), \\ a_0^3 M[\omega_{11}MM'' + M^2((\omega_{12}+\omega_{13})\Phi^2 + \omega_{13}\Psi) + \omega_{14}\Phi MM' + \omega_{15}M'^2] + O(M^2), \end{cases} \tag{B 6a}$$

https://doi.org/10.1017/jfm.2020.775 Published online by Cambridge University Press

$$u_{tx} = \begin{cases} -\dfrac{Q_2}{2\rho_0 a_0^2} + O(\varepsilon_w^0), \\ a_0^2[\omega_{16} MM'' + M^2((\omega_{17}+\omega_{18})\Phi^2 + \omega_{18}\Psi) + \omega_{19}\Phi MM' + \omega_{20}M'^2] + O(M), \end{cases} \tag{B 6b}$$

$$u_{xx} = \begin{cases} \dfrac{Q_2}{2\rho_0 a_0^3} + O(\varepsilon_w^0), \\ \dfrac{a_0}{M}[\omega_{41} MM'' + M^2((\omega_{42}+\omega_{43})\Phi^2 + \omega_{43}\Psi) + \omega_{44}\Phi MM' + \omega_{45}M'^2] + O(M^0), \end{cases} \tag{B 6c}$$

$$\rho_{tt} = \begin{cases} \dfrac{Q_2}{2a_0^2} + O(\varepsilon_w^0), \\ \rho_0 a_0^2[\omega_{21} MM'' + M^2((\omega_{22}+\omega_{23})\Phi^2 + \omega_{23}\Psi) + \omega_{24}\Phi MM' + \omega_{25}M'^2] + O(M), \end{cases} \tag{B 7a}$$

$$\rho_{tx} = \begin{cases} -\dfrac{Q_2}{2a_0^3} + O(\varepsilon_w^0), \\ \dfrac{\rho_0 a_0}{M}[\omega_{26} MM'' + M^2((\omega_{27}+\omega_{28})\Phi^2 + \omega_{28}\Psi) + \omega_{29}\Phi MM' + \omega_{30}M'^2] + O(M), \end{cases} \tag{B 7b}$$

$$a_{tt} = \begin{cases} \dfrac{(\gamma-1)Q_2}{4\rho_0 a_0} + O(\varepsilon_w^0), \\ -a_0^3 M[\omega_{31} MM'' + M^2((\omega_{32}+\omega_{33})\Phi^2 + \omega_{33}\Psi) + \omega_{34}\Phi MM' + \omega_{35}M'^2] + O(M), \end{cases} \tag{B 8a}$$

$$a_{tx} = \begin{cases} -\dfrac{(\gamma-1)Q_2}{4\rho_0 a_0^2} + O(\varepsilon_w^0), \\ a_0^2[\omega_{36} MM'' + M^2((\omega_{37}+\omega_{38})\Phi^2 + \omega_{38}\Psi) + \omega_{39}\Phi MM' + \omega_{40}M'^2] + O(M), \end{cases} \tag{B 8b}$$

where $\omega_{1,2,\ldots,45}$ are constant functions of γ given in table 2 in appendix A.

Appendix C. Derivation of the Q_2 initial condition

Here we provide detailed steps towards the derivation of (4.12), the initial condition of Q_2 associated with the piston-generated shock.

From the kinematic condition of (4.7*b*), the initial jerk of flow between the piston surface and the shock is related to the initial values of partial derivatives u_t, u_x, u_{tt}, u_{tx} and u_{xx} given in (B 1)–(B 4) and (B 5)–(B 8). Particularly, in the strong-shock limit, the M' and M'' dependences of these derivatives can be expanded using (3.17) and (3.26) to give expressions in terms of M, Q_1, Q_2, Φ and Ψ. As a result, solving (4.7*b*) for Q_2 and evaluating at $t = 0^+$ gives, for $M \to \infty$,

$$\begin{aligned} Q_2(\beta, 0^+) = \big\{ & -\zeta_2[\Phi(\iota_1 M^2 + \iota_2 u_0^2 + \iota_3 u_0 M)M^3 Q_1 - (\iota_4 u_0^2 - \iota_5 M^2 + \iota_6 u_0 M)Q_1^2] \\ & - M^6[(\iota_7\Phi^2 + 2\iota_8\Psi)u_0 M + (\iota_9\Phi^2 + \iota_{10}\Psi)M^2 + (\iota_{11}\Phi + \iota_{12}\Psi)u_0^2] \\ & + M^5 \ddot{u}_0 \big\}_{t=0^+} / [\zeta_2\gamma_4 M^2(\omega_{11}M^2 + 2\omega_{16}u_0 M + \omega_{41}u_0^2)]_{t=0^+}, \end{aligned} \tag{C 1}$$

https://doi.org/10.1017/jfm.2020.775 Published online by Cambridge University Press

where $\iota_{1,2,\ldots,12}$ and $\omega_{11,16,41}$ are coefficients given in table 2 in appendix A. Here the initial value of Ψ remains to be determined. This is achieved by substituting the perturbed shock profile (4.4), together with $\Phi(\beta, 0^+)$ found in (4.9), into its definition (3.22), implying that

$$\Psi(\beta, 0^+) = -\frac{\epsilon^2 \sin^2(\beta)(\epsilon^2 \cos(2\beta) + 2\epsilon^2 + 1)}{(\epsilon^2 \sin^2(\beta) + 1)^3}. \tag{C 2}$$

Similarly for the weak-shock limit, expanding (4.7*b*) and solving for Q_2 directly gives, for $M \to 1$,

$$Q_2(\beta, 0^+) = \frac{2\ddot{u}_0}{(u_0 - 1)^2} + \frac{4(3\gamma - 1)\Phi(M - 1) + (\gamma + 1)^2 Q_1}{2(\gamma + 1)^4 (u_0 - 1)^2}\bigg|_{t=0^+} \big\{(\gamma + 1)^2 Q_1 \times (2(M - 1) - u_0 + 1) + 4\Phi(M - 1)[2(\gamma - 1) - (3\gamma - 1)u_0]\big\}_{t=0^+}. \tag{C 3}$$

Now substituting (4.6), (4.8), (4.9) and (C 2) into both (C 1) and (C 3) prepares the full expression of $Q_2(\beta, 0^+)$ in terms of the parameters M_0, ϵ and $\ddot{u}_0(\beta)$. Setting $\epsilon = 0$ then produces

$$Q_2(\beta, 0^+)|_{\epsilon=0} = \begin{cases} \dfrac{M_0 \ddot{u}_0}{\gamma_4 \zeta_2 (\omega_{11} + 2\alpha_1 \omega_{16} + \alpha_1^2 \gamma_4)}, & M_0 \to \infty, \\ \dfrac{2(\gamma + 1)^2 \ddot{u}_0}{(5 + \gamma - 4M_0)^2}, & M_0 \to 1, \end{cases} \tag{C 4}$$

which must vanish as required by the unperturbed uniform flow condition. Therefore, one demands $\ddot{u}_0 = 0$, suggesting that the initial flow attached to the piston has zero acceleration and jerk. Finally, for small ϵ, (C 1) and (C 3) are Taylor-expanded to give the leading-order powers shown in (4.12):

$$Q_2(\beta, 0^+) \sim \begin{cases} (\xi_1 \cos^2(\beta) + \xi_2 \sin^2(\beta)) M_0^4 \epsilon^2, & M_0 \to \infty, \\ -\dfrac{32\gamma \cos^2(\beta)(M_0 - 1)^3 \epsilon^2}{(\gamma + 1)^3}, & M_0 \to 1. \end{cases} \tag{C 5}$$

Appendix D. An edge-detection algorithm

The specific edge-detection algorithm used in § 5 that searches for the onset of a discontinuity on discrete values of the periodic function $M(\beta, t)$ is briefly outlined in this section. The algorithm is taken from a family of spectral methods developed by Gelb & Tadmor (2000, 2006).

At each time step, discrete data for the Mach-number profile, $\bar{M}_j$, subject to the rescaling $\min_j(\bar{M}_j) = 0$ and $\max_j(\bar{M}_j) = 1$, is obtained first on the size $2N$ uniform grid $\beta_j = 2\pi j/(2N + 1)$, where $j = 0, 1, \ldots, 2N$. The discrete concentration detector is defined as

$$\tilde{T}_N^c[\bar{M}](\beta) = \pi \mathrm{i} \sum_{k=-N}^{N} \mathrm{sgn}(k)\, c\left(\frac{|k|\Delta\beta}{\pi}\right) \tilde{M}_k \exp(\mathrm{i}k\beta), \tag{D 1}$$

where $\tilde{M}_k$ are the Fourier coefficients,

$$\tilde{M}_k = \frac{1}{2N + 1} \sum_{j=0}^{2N} \bar{M}_j \exp(-\mathrm{i}k\beta_j), \tag{D 2}$$

https://doi.org/10.1017/jfm.2020.775 Published online by Cambridge University Press

and $c(s_k)$ with $s_k = |k|\Delta\beta/\pi$ is the concentration factor. The following two admissible concentration factors are considered next: the first-order polynomial factor,

$$c^{pol}(s_k) = \sin\left(\frac{\pi s_k}{2}\right), \tag{D 3}$$

and the exponential factor,

$$c^{exp}(s_k) = \sin\left(\frac{\pi s_k}{2}\right)\exp\left(\frac{1}{\alpha s_k(s_k-1)}\right)\left(\int_0^1 \exp\left(\frac{1}{\alpha s(s-1)}\right)\mathrm{d}s\right)^{-1}, \tag{D 4}$$

where $\alpha = 6$ is chosen (Gelb & Cates 2008). By invoking the minmod operator,

$$\mathrm{minmod}(f_1, f_2) = \begin{cases} \min(f_1, f_2), & \text{if } f_1, f_2 > 0, \\ \max(f_1, f_2), & \text{if } f_1, f_2 < 0, \\ 0, & \text{otherwise}, \end{cases} \tag{D 5}$$

the two concentration factors can be combined to give

$$\tilde{T}_N^{minmod}[\bar{M}](\beta) = \mathrm{minmod}(\tilde{T}_N^{pol}[\bar{M}](\beta),\ \tilde{T}_N^{exp}[\bar{M}](\beta)). \tag{D 6}$$

The concentration factors c are chosen such that all three aforementioned discrete detectors $\tilde{T}_N^c$ converge to the desired limit that selects jump discontinuities, i.e. $\lim_{\delta\to 0}[\bar{M}(\beta+\delta) - \bar{M}(\beta-\delta)]$, for all $\beta \in [0, 2\pi)$ as $N \to \infty$. The separation of scales achieved by these discrete detectors is further enhanced by the nonlinear function

$$E_{q,N} = N^{q/2}(\tilde{T}_N^{minmod}[\bar{M}](\beta))^q, \tag{D 7}$$

for some $q > 1$. This leads to the enhanced concentration method

$$E_N^{minmod}[\bar{M}](\beta) = \begin{cases} \tilde{T}_N^{minmod}[\bar{M}](\beta), & \text{if } |E_{q,N}| > J_{crit}, \\ 0, & \text{if } |E_{q,N}| > J_{crit}, \end{cases} \tag{D 8}$$

where $J_{crit} \sim O(1)$ is a global threshold below which jump discontinuities are neglected. The minmod detector is chosen here for its better performance locating discrete jumps to the nearest grid point while removing spurious oscillations.

REFERENCES

BATES, J. W. 2012 On the theory of a shock wave driven by a corrugated piston in a non-ideal fluid. *J. Fluid Mech.* **691**, 146–164.

BATES, J. W. 2015 Theory of the corrugation instability of a piston-driven shock wave. *Phys. Rev.* E **91** (1), 1–6.

BEST, J. P. 1991 A generalisation of the theory of geometrical shock dynamics. *Shock Waves* **1** (4), 251–273.

BEST, J. P. 1993 Accounting for transverse flow in the theory of geometrical shock dynamics. *Proc. R. Soc. Lond.* A **442** (1916), 585–598.

BRISCOE, M. G. & KOVITZ, A. A. 1968 Experimental and theoretical study of the stability of plane shock waves reflected normally from perturbed flat walls. *J. Fluid Mech.* **31** (3), 529–546.

CLAVIN, P. 2013 Nonlinear analysis of shock–vortex interaction: mach stem formation. *J. Fluid Mech.* **721**, 324–339.

https://doi.org/10.1017/jfm.2020.775 Published online by Cambridge University Press

CLAVIN, P. & DENET, B. 2002 Diamond patterns in the cellular front of an overdriven detonation. *Phys. Rev. Lett.* **88** (4), 044502.

COURANT, R. & FRIEDRICHS, K. O. 1999 *Supersonic Flow and Shock Waves*, vol. 21. Springer Science and Business Media.

DENET, B., BIAMINO, L., LODATO, G., VERVISCH, L. & CLAVIN, P. 2015 Model equation for the dynamics of wrinkled shockwaves: comparison with DNS and experiments. *Combust. Sci. Technol.* **187** (1–2), 296–323.

DRAKE, R. P., GLENDINNING, S. G., ESTABROOK, KENT, REMINGTON, B. A., MCCRAY, RICHARD, WALLACE, R. J., SUTER, L. J., SMITH, T. B., CARROLL, J. J., LONDON, R. A. *et al.* 1998 Observation of forward shocks and stagnated ejecta driven by high-energy-density plasma flow. *Phys. Rev. Lett.* **81** (10), 2068–2071.

D'YAKOV, S. P. 1954 Shock wave stability. *Zh. Eksp. Teor. Fiz.* **27** (3), 288–295.

EGGERS, J., GRAVA, T., HERRADA, M. A. & PITTON, G. 2017 Spatial structure of shock formation. *J. Fluid Mech.* **820**, 208–231.

EMANUEL, G. 2016 *Analytic Fluid Dynamics*, 3rd edn. CRC Press.

EMANUEL, G. 2019 Derivatives on the downstream side of a moving, curved shock. *J. Engng Maths* **117** (1), 79–105.

FARIA, L. M., KASIMOV, A. R. & ROSALES, R. R. 2015 Theory of weakly nonlinear self-sustained detonations. *J. Fluid Mech.*

FREEMAN, N. C. 1955 A theory of the stability of plane shock waves. *Proc. R. Soc. Lond.* A **228** (1174), 341–362.

FREEMAN, N. C. 1957 On the stability of plane shock waves. *J. Fluid Mech.* **2** (4), 397–411.

GELB, A. & CATES, D. 2008 Detection of edges in spectral data III–refinement of the concentration method. *J. Sci. Comput.* **36** (1), 1–43.

GELB, A. & TADMOR, E. 2000 Detection of edges in spectral data II. Nonlinear enhancement. *SIAM J. Numer. Anal.* **38** (4), 1389–1408.

GELB, A. & TADMOR, E. 2006 Adaptive edge detectors for piecewise smooth data based on the minmod limiter. *J. Sci. Comput.* **28** (2–3), 279–306.

HOEFER, M. A., ABLOWITZ, M. J. & ENGELS, P. 2008 Piston dispersive shock wave problem. *Phys. Rev. Lett.* **100** (8), 084504.

HORNUNG, H. G. 2010 Deriving features of reacting hypersonic flow from gradients at a curved shock. *AIAA J.* **48** (2), 287–296.

KANWAL, R. P. 1957 Determination of the vorticity and the gradients of flow parameters behind a three-dimensional unsteady curved shock wave. *Arch. Rat. Mech. Anal.* **1** (1), 225–232.

KATKO, B. J., CHAVEZ, R., LIU, H., LAWLOR, B., MCGUIRE, C., ZHENG, L., ZANTESON, J. & ELIASSON, V. 2020 Experimental and numerical study of blast-structure interaction. In *Structures Congress 2020*, pp. 105–118. American Society of Civil Engineers.

LAPWORTH, K. C. 1959 An experimental investigation of the stability of plane shock waves. *J. Fluid Mech.* **6** (3), 469–480.

LELE, S. K. 1992 Compact finite difference schemes with spectral-like resolution. *J. Comput. Phys.* **103** (1), 16–42.

LIGHTHILL, M. J. 1949 The diffraction of blast. I. *Proc. R. Soc. Lond.* A **198** (1055), 454–470.

LIGHTHILL, M. J. 1950 The diffraction of blast. II. *Proc. R. Soc. Lond.* A **200** (1063), 554–565.

LINDL, J., LANDEN, O., EDWARDS, J., MOSES, E., NIC TEAM 2014 Review of the national ignition campaign 2009–2012. *Phys. Plasmas* **21** (2), 020501.

LODATO, G., VERVISCH, L. & CLAVIN, P. 2016 Direct numerical simulation of shock wavy-wall interaction: analysis of cellular shock structures and flow patterns. *J. Fluid Mech.* **789**, 221–258.

LODATO, G., VERVISCH, L. & CLAVIN, P. 2017 Numerical study of smoothly perturbed shocks in the newtonian limit. *Flow Turbul. Combust.* **99** (3-4), 887–908.

MAJDA, A. & ROSALES, R. 1983 A theory for spontaneous mach stem formation in reacting shock fronts, I. The basic perturbation analysis. *SIAM J. Appl. Math.* **43** (6), 1310–1334.

MATSUI, N., MIMA, K., HONDA, M. & NISHIGUCHI, A. 1999 Analysis of rippled shock-wave propagation and ablation-front stability by theory and hydrodynamic simulation. *J. Plasma Phys.* **61** (1), 43–50.

https://doi.org/10.1017/jfm.2020.775 Published online by Cambridge University Press

MAXWELL, A., DRYER, M. & MCINTOSH, P. 1985 A piston-driven shock in the solar corona. *Solar Phys.* **97** (2), 401–413.

MÖLDER, S. 2016 Curved Shock Theory. *Shock Waves* **26** (4), 337–353.

MOSTERT, W, PULLIN, D. I., SAMTANEY, R. & WHEATLEY, V. 2017 Geometrical shock dynamics for magnetohydrodynamic fast shocks. *J. Fluid Mech.* **811**, R2.

MOSTERT, W., PULLIN, D. I., SAMTANEY, R. & WHEATLEY, V. 2018*a* Singularity formation on perturbed planar shock waves. *J. Fluid Mech.* **846**, 536–562.

MOSTERT, W., PULLIN, D. I., SAMTANEY, R. & WHEATLEY, V. 2018*b* Spontaneous singularity formation in converging cylindrical shock waves. *Phys. Rev. Fluids* **3** (7), 071401.

PANT, J. C. 1969 Some aspects of unsteady curved shock waves. *Intl J. Engng Sci.* **7** (2), 235–245.

STREHLOW, R. A. & FERNANDES, F. D. 1965 Transverse waves in detonations. *Combust. Flame*. **9** (2), 109–119.

THOMAS, T. Y. 1947 On curved shock waves. *J. Maths Phys.* **26** (1–4), 62–68.

VAN MOORHEM, W. K. & GEORGE, A. R. 1975 On the stability of plane shocks. *J. Fluid Mech.* **68** (1), 97–108.

WAN, Q., JEON, H., DEITERDING, R. & ELIASSON, V. 2017 Numerical and experimental investigation of oblique shock wave reflection off a water wedge. *J. Fluid Mech.* **826**, 732–758.

WHITHAM, G. B. 1957 A new approach to problems of shock dynamics. Part 1. Two-dimensional problems. *J. Fluid Mech.* **2** (2), 145–171.

WHITHAM, G. B. 2011 *Linear and Nonlinear Waves*, vol. 42. John Wiley and Sons.

ZAIDEL, R. M. 1967 Development of perturbations in plane shock waves. *J. Appl. Mech. Tech. Phys.* **8**, 20–25.

https://doi.org/10.1017/jfm.2020.775 Published online by Cambridge University Press